國立交通大學

光電工程研究所

碩士論文

以非晶矽鍺碳發展之薄膜堆疊型太陽能電池

Tandem Solar Cell Developed by Amorphous Thin Film Silicon Alloyed with Germanium and Carbon

研 究 生：許智維

指導教授：謝嘉民、郭浩中

中 華 民 國 九 十 九 年 七 月

利用高密度電漿於低溫製作非晶矽/微晶矽薄膜太陽能電池

Fabrication of amorphous/microcrystalline silicon thin film solar cells at low temperature by high density plasma

研 究 生： 許智維　　Student： Yu-Hsin Lin

指導教授： 謝嘉民　　Advisor： Jia-Min Shieh

郭浩中　　Hao-Chung Kuo

國 立 交 通 大 學

光電工程研究所

碩 士 論 文

A Thesis

Submitted to Department of Photonics

College of Electrical Engineering and Computer Science

National Chiao Tung University

in partial Fulfillment of the Requirements

for the Degree of

Master

in

Electro-Optical Engineering

June 2010

Hsinchu, Taiwan, Republic of China

中華民國九十九年七月

以非晶矽鍺碳發展之薄膜堆疊型太陽能電池

學生:許智維　　指導教授:謝嘉民

郭浩中

國立交通大學光電工程研究所碩士班

摘要

本論文之研究利用高密度電漿化學氣相沉積系統低溫、高解離率等優點製備低缺陷密度之氫化非晶矽薄膜，發展參雜鍺和碳之氫化非晶矽(a-Si, a-SiGe, a-SiC)調變能隙漸變之矽薄膜太陽能電池。由於氫化非晶矽薄膜能隙較高(1.8~1.9eV)，氫化非晶矽薄膜太陽能電池有高開路電壓的優點，但相對在太陽光譜中長波長的部分(750nm 以上)無法有效吸收而造成短路電流密度較低。為了克服上述氫化非晶矽薄膜太陽能電池之缺點，我們開發非晶矽基能隙漸變薄膜 a-Si_xGe_{1-x} (1.4~1.6eV) 、Si_yC_{1-y}(1.9~2.0eV)，使其可吸收太陽光譜中不同波段的，有效的增強光伏特元件吸收寬頻太陽光能的利用率，並且可以以各種不同能隙所製備的矽薄膜太陽能電池為基礎發展多接面堆疊型太陽能電池，吸收可見光中各個不同波段的光，並且具有較高的開路電壓(2.0~2.3V)。本實驗室目前已經開發出各種不同能隙知單接面氫化非晶矽太陽能電池，其中單接面氫化非晶矽薄膜太陽能電池轉換效率達8.7%，矽鍺薄膜太陽能電池轉換效率約 7%，碳化矽薄膜太陽能電池轉換效率也已經達到約 8%的高效率成果，且從量子效率量測結果可看出和非晶矽

太陽能電池相比矽鍺薄膜太陽能電池在 700~850nm 以及碳化矽薄膜太陽能電池在 350~500nm 皆有顯著的提升。而堆疊型太陽能電池的部分，我們目前已經開發了雙層和三層堆疊型太陽能電池，其中 a-Si/a-Si 以及 a-Si/a-SiGe 雙層堆疊型薄膜太陽能電池開路電壓分別可達到 1.6 以及 1.4V，a-Si/a-Si/a-SiGe 三層堆疊型太陽能電池開路電壓為 2.07 V，目前已經可以將多個太陽能堆疊起來在電壓的表現有很好的串接效果，而 a-Si/a-Si 以及 a-Si/a-SiGe 雙層堆疊型薄膜太陽能電池轉換效率則分別為 6.5%和 5%，三層的堆疊型太陽能電池轉換效率 3.5%，未來研究的方向將致力於改善堆疊型太陽能電池各接面間的穿隧接面，以提高堆疊型太陽能電池之短路電流進而提升轉換效率。

Tandem Solar Cell Developed by Amorphous Thin Film Silicon Alloyed with Germanium and Carbon

Student: Chih-Wei, Hsu Advisor: J.M., Shieh

H.C., Kuo

National Chiao Tung University, Department of Photonics

Abstract

We have fabricated silicon-based alloy thin film solar cell by using high density plasma method. The high dissociation capacity of HDPCVD can be used to yield high-density plasma and markedly increased electron temperature, promoting the diffusion capability of the reactive radicals and eventually yielding low-defect a-Si films at low temperatures. Due to high optical band gap of amorphous silicon thin film, a-Si thin film solar cell shows the property of high open circuit voltage. But, this feature also limit the absorption in the near infrared part of solar spectra, so the short circuit current density is much lower compared with amorphous silicon germanium and microcrystal thin film silicon solar cell. In order to overcome the above-mentioned shortcomings, we utilize the amorphous silicon-based alloy, which are a-Si_xGe_{1-x} (1.4~1.6eV) and Si_yC_{1-y}(1.9~2.0eV), to engineer the optical bandgap. The thin films with different optical bandgap could absorb the different part in solar spectra. Thus, we can effectively take advantage of the full solar spectra. And we can also develop muti-junction thin film solar cell based in the thin film solar cells. Each junctions of muti-junction solar cell have different optical bandgap, so they could absorb different part of solar spectra. Furthermore, the muti-junction solar cell has higher open voltage(2.0~2.3V). Currently, we have demonstrated single

junction a-Si, a-SiGe and a-SiC thin film solar cell with conversion efficiency achieving 8.7%, 7% and 8%, respectively. Compared with a-si thin film solar cell, the quantum efficiency of a-SiGe and a-SiC significantly increased in 700~850nm and 350~500nm. Besides, we have also demonstrated double junctions solar cell, including a-Si/a-Si and a-Si/a-SiGe tandem solar cell and triple junction solar cell. The open circuit voltage of a-Si/a-Si, a-Si/a-SiGe tandem solar cells and a-Si/a-Si/a-SiGe triple junction solar cell is 1.6V, 1.4V and 2.07V respectively. The muti-junction we mentioned above have successful performance in open circuit voltage. Conversion efficiency of a-Si/a-Si , a-Si/a-SiGe and a-Si/a-Si/a-SiGe muti-junction solar cell tandem solar cell is 6.5%, 5% and 3.5% respectively. In the future, my research will focus on tunneling junction to reduce the recombination and upgrade short circuit performance.

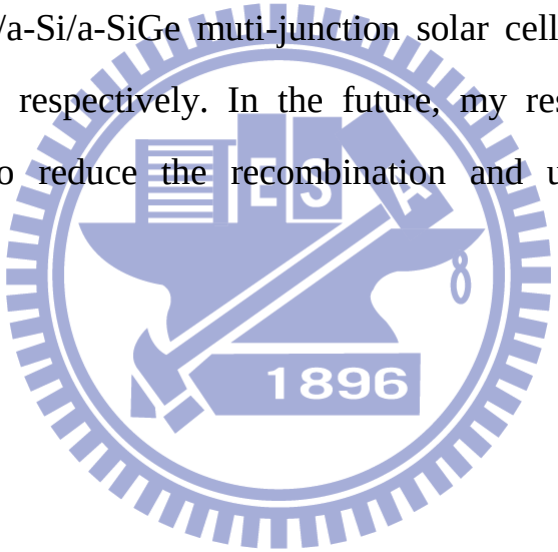

誌謝

經過碩班兩年的努力，終於到了開花結果的時候了，本論文得以順利完成，首先非常感謝我的指導老師謝嘉民教授與郭浩中教授，老師的細心指導不僅在專業知識上讓我獲益匪淺，在思考與解決問題的能力也有突破性的進步，同時也感謝我的口試委員黃中垚教授、戴寶通博士、沈昌宏博士對於本論文的教導與指正，使本論文更臻完善。

感謝奈米元件實驗室工程師黃文賢、王昭凱、游文謙、陳彥佑、林耿正、林鈺閔，你們在實驗儀器上的指導使得我更懂得如何操作儀器。。

感謝這兩年和我共同奮鬥的同學們育新、泓瑜、皇彥、國欽、俊凱，以及世杰、良豪、大頭、卡卡等學弟妹，有了你們的陪伴讓我的碩班生涯更加多采多，使我能順利的完成研究。祝福你們未來在實驗上事事順利。

在此還要感謝我的父母給我精神上的支持，你們的鼓勵使我有能夠堅定我的信心。

Table of Contents

摘要 i

Abstract iii

Table of Contents vi

Figure Content viii

Chapter 1 Introduction and motivation 1

1.1 Introduction of various type of Solar Cell 2
Crystalline Silicon 2
Silicon thin films 2
Gallium arsenide multijunction 3
Cadmium telluride solar cell 4
Copper indium gallium selenide solar cell 5
Dye-sensitized solar cells 6
Organic/polymer solar cells 7
1.2 The Market of Solar Cell 9

Chapter 2 Priciple of Semiconductor Solar Cells 11

2.1 Solar Radiation 11
2.2 PN Junction in Equilibrium 14
2.3 Under Illumination 20

Chapter 3 Experiment Instrument & Measurement System 25

3.1 High Density Plasma Chemical Vapor Deposition System 25
3.2 E-Gun Evaporator Deposition System 26
3.3 DC Magnetrons Sputter Deposition 27
3.4 N&K Analyzer 28
3.5 UV-Visible Spectroscopy 28
3.6 Solar Simulator 29
3.7 QE Measurement 31

Chapter 4 Device Fabrication Process and Growth Mechanism 32

4.1 Device Fabrication Process 32
4.2 Thin Film Growth Mechanism 35

Chapter 5 Experiment Result and Discussion 36

5.1 Thin Film Analysis 36
5.1.1 The Growth Condition of Each Layers Fabricated by HDPCVD 36
5.1.2 Material Structure and Optical Characteristic 37
5.2 Amorphous Silicon and Silicon Germanium Alloy Single Junction Solar Cell 50
5.2.1 Amorphous Silicon Thin Film Solar Cell 50
5.2.2 Amorphous Silicon Germanium Thin Film Solar Cell 52
5.2.3 Amorphous Silicon Carbide Thin Film Solar Cell 61
5.3 Double Junction and Triple Junction Solar Cell 64
5.3.1 a-Si/a-Si Tandem Solar Cell 64
5.3.2 a-Si/a-SiGe Tandem Solar Cell 66
5.3.3 a-Si/a-Si/a-SiGe Triple Junction Solar Cell 70
5.4 Conclusion and Future Work 72

Reference 73

Figure Content

Figure 1 Category of Solar Cells 8
Figure 2 Comparison of Different Type of Solar Production 9
Figure 3 The Growth Trend of Thin Films and Crystalline Silicon Solar Cell over the Years ... 10
Figure 4 The Zenith Angle of the Sun 13
Figure 5 Solar Spectrum at Different Air-Mass Conditions 13
Figure 6 Solar Spectrum in Photon Flux Density per Photon Energy for AM0 and AM1.5 Conditions 14
Figure 7 The electric field and forces acting on the charged carrier in the space charge region 15
Figure 8 Energy band diagram of a pn junction in thermal equilibrium 16
Figure 9 The space charge density, electric field, and electric field potential through the space charge region of a uniformly doped pn junction 17
Figure 10 Minority carrier concentrations in a pn junction under forward bias. 18
Figure 11 Ideal I-V characteristic of a pn junction diode. 20
Figure 12 Operation of Solar Cell 20
Figure 13 Equivalent Circuit of pn Solar Cell (a) without (b) with parallel and series resistance 22
Figure 14 Illuminated I-V Characteristic 22
Figure 15 Effect of (a) incrising series and (b) reducing parallel resistances. In each case the outer curve has Rs=0 .and Rsh=∞ 24
Figure 16 The High Density Plasma Chemical Vapor Deposition System 26
Figure 17 E-gun Evaporator Deposition System 27
Figure 18 Solar Simulator System and I-V Measurement 30
Figure 19 Probe Station with Flip Function 30
Figure 20 typical a-Si:H n&K corresponds to wavelength and photon energy 37
Figure 21 Refractive Index and Extinction Coefficient of p-layer Corresponds to Wavelength 38
Figure 22 Refractive Index and Extinction Coefficient of i-layer Corresponds to Wavelength 39
Figure 23 Refractive Index and Extinction Coefficient of n-layer Corresponds to Wavelength 40
Figure 24 P-layer Absorption Coefficient Corresponds to the Photon Energy and Optical band gap fitting by Tauc Plot 41
Figure 25 I-layer Absorption Coefficient Corresponds to the Photon Energy and Optical band gap fitting by Tauc Plot 41
Figure 26 N-layer Absorption Coefficient Corresponds to the Photon Energy and Optical band

gap fitting by Tauc Plot 42
Figure 27 SiH_4-GeH_4:H_2=14-1:150 power=40w optical bandgap fitting 43
Figure 28 SiH_4-GeH_4:H_2=13-2:200 power=40w optical bandgap fitting 43
Figure 29 SiH_4-GeH_4:H_2=12-3:400 power=40w optical bandgap fitting 44
Figure 30 SiH_4-GeH_4:H_2=10-2:200 power=40w optical bandgap fitting 44
Figure 31 SiH_4-GeH_4:H_2=10-2:200 power=30w optical bandgap fitting 45
Figure 32 SiH_4-GeH_4:H_2=10-2:200 power=40w optical bandgap fitting 46
Figure 33 SiH_4-GeH_4:H_2=9-3:200 power=40w optical bandgap fitting 46
Figure 34 SiH_4-GeH_4:H_2=9-3:400 power=40w optical bandgap fitting 47
Figure 35 SiH_4-GeH_4:H_2=8-4:200 power=40w optical bandgap fitting 47
Figure 36 SiH_4-GeH_4:H_2=8-4:400 power=40w optical bandgap fitting 48
Figure 37 SiH_4-GeH_4:H_2=8-4:400 power=40w optical bandgap fitting 48
Figure 38 SiH_4-GeH_4:H_2=6-6:600 power=40w optical bandgap fitting 49
Figure 39 Growth Rate and GeH_4/SiH_4+GeH_4 Ratio 49
Figure 40 Structure of a-Si:H Thin Film Solar Cell 50
Figure 41 Voc, Jsc, FF and Conversion Efficiency of Each Size of Solar Cell 51
Figure 42 TEM Graph and Diffraction Pattern of a-Si Thin Film Solar Cell 51
Figure 43 The Structure of a-SiGe:H Thin Film Solar Cell 52
Figure 44 I-V Curve of a-SiGe Thin Film Solar Cell by Varying GeH_4/SiH_4+GeH_4 Ratio 53
Figure 45 The QE of a-SiGe thin film solar cell by varying GeH_4/SiH_4+GeH_4 ratio 54
Figure 46 I-V Curve of a-SiGe Thin Film Solar Cell by Varying H_2 Inflow 55
Figure 47 QE Response of a-SiGe Thin Film Solar Cell by Varying H_2 Inflow 56
Figure 48 I-V Curve of a-SiGe Thin Film Solar Cell by Varying pressure and power 58
Figure 49 QE responds of a-SiGe Thin Film Solar Cell by Varying pressure and power 58
Figure 50 I-V Curve of a-SiGe Thin Film Solar Cell by Varying thickness and pressure 59
Figure 51 QE Responds of a-SiGe Thin Film Solar Cell by Varying pressure and Thicknesss 59
Figure 52 Structure of a-SiC:H Thin Film Solar Cell 61
Figure 53 I-V Curve of a-SiC:H Thin Film Solar Cell 62
Figure 54 QE Responds of a-SiC:H Thin Film Solar Cell 63
Figure 55 Structure of a-Si/a-Si Tandem Solar Cell 64
Figure 56 I-V curve of a-Si/a-Si Tandem Solar Cell 65
Figure 57 Structure of a-Si/a-SiGe Tandem Solar Cell 67
Figure 58 I-V Curve of a-Si/a-SiGe Tandem Solar Cell Varying the GeH_4/SiH_4+GeH_4 Ratio on Bottom Cell 67
Figure 59 I-V Curve of a-Si/a-SiGe Tandem Solar Cell Varying i-layer Thickness on Top Cell 69
Figure 60 Structure of a-Si/a-Si/a-SiGe Triple Junction Solar Cell 70
Figure 61 I-V Curve of a-Si/a-Si/a-SiGe Triple Junction Solar Cell 71

Chapter 1

Introduction and motivation

Solar cells, at the present time, furnish the most-important long-duration power supply in small-scale terrestrial and space applications such as satellites and space vehicles. As worldwide energy demand increases, conventional energy resources such as fossil fuels, will be exhausted within the next century. Therefore, we must develop and use alternative energy resources, especially our only long-term natural resource-the sun. The solar cell is considered a major candidate for obtaining energy from the sun, since it can convert sunlight directly to electricity with high conversion efficiency (as opposed to extracting thermal energy). It can provide nearly permanent power at low operating cost, and is virtually free of pollution. Recently, research and development of low-cost flat-panel solar panels, thin-film devices, concentrator systems, and many innovative concepts have increased. In the near future, the costs of small solar-power modular units and solar-power plants will be economically feasible for large-scale production and use of solar energy. In this chapter, I would introduce the categories, market, brief history of solar cell and my motivation to do the research in amorphous thin film solar cells[1].

1.1 Introduction of various type of Solar Cell

There are many different kinds of solar cells which contain a light absorbing layer with different material contained within the cell structure to absorb photons and generate electrons via the photovoltaic effect. The materials used in solar cells tend to have the property of preferentially absorbing the wavelengths of solar light that reach the Earth surface. However, some solar cells are optimized for light absorption beyond Earth's atmosphere as well. Light absorbing materials can often be used in multiple physical configurations to take advantage of different light absorption and charge separation mechanisms. The photovoltaic can be classified as the following (see **Figure 1**).

Crystalline Silicon

Bulk silicon is separated into two categories according to crystallinity and crystal size in the resulting ingot or wafer.

1. **Monocrystalline Silicon (c-Si)**: often made using the Czochralski process. Single-crystal wafer cells tend to be expensive, and because they are cut from cylindrical ingots, do not completely cover a square solar cell module without a substantial waste of refined silicon. Hence most c-Si panels have uncovered gaps at the four corners of the cells.
2. **Poly Silicon (poly-Si):** made from cast square ingots — large blocks of molten silicon carefully cooled and solidified. Poly-Si cells are less expensive to produce than single crystal silicon cells, but are less efficient.

Silicon thin films

Silicon thin-film cells are mainly deposited by chemical vapor deposition (typically

plasma-enhanced (PE-CVD)) from silane gas and hydrogen gas. Depending on the deposition parameters, this can yield

1. **Amorphous silicon (a-Si or a-Si:H)**

   Amorphous silicon has a higher bandgap (1.7~1.9 eV) than crystalline silicon (c-Si) (1.1 eV), which means it absorbs the visible part of the solar spectrum more strongly than the infrared portion of the spectrum. Because of this feature, a-Si thin film solar cell has higher open circuit voltage which is about 0.9V.

2. **Microcrystalline silicon (uc-Si or uc-Si:H)**

   Microcrystalline silicon has about the same bandgap as c-Si, the uc-Si and a-Si can advantageously be combined in thin layers, creating a layered cell called a tandem cell. The top cell in a-Si absorbs the visible light and leaves the infrared part of the spectrum for the bottom cell in nc-Si. These structures make use of some of the same thin-film light absorbing materials but are overlain as an extremely thin absorber on a supporting matrix of conductive polymer or mesoporous metal oxide having a very high surface area to increase internal reflections (and hence increase the probability of light absorption). Using microcrystals allows one to design architectures on the length scale of nanometers, the typical exciton diffusion length. In particular, single-microcrystal ('channel') devices, an array of single p-n junctions between the electrodes and separated by a period of about a diffusion length, represent a new architecture for solar cells and potentially high efficiency.

Gallium arsenide multijunction

The gallium arsenide multijunction cells consist of multiple thin films produced using metalorganic vapour phase epitaxy. A triple-junction cell, for example, may consist of the semiconductors: GaAs, Ge, and $GaInP_2$. Each type of semiconductor will have a characteristic

band gap energy which, loosely speaking, causes it to absorb light most efficiently at a certain color, or more precisely, to absorb electromagnetic radiation over a portion of the spectrum. The semiconductors are carefully chosen to absorb nearly all of the solar spectrum, thus generating electricity from as much of the solar energy as possible. GaAs based multijunction devices are the most efficient solar cells to date, reaching a record high of 40.7% efficiency under "500-sun" solar concentration and laboratory conditions. This technology is currently being utilized in the Mars rover missions.Tandem solar cells based on monolithic, series connected, gallium indium phosphide (GaInP), gallium arsenide GaAs, and germanium Ge pn junctions, are seeing demand rapidly rise. In just the past 12 months (12/2006 - 12/2007), the cost of 4N gallium metal has risen from about $350 per kg to $680 per kg. Additionally, germanium metal prices have risen substantially to $1000–$1200 per kg this year. Those materials include gallium (4N, 6N and 7N Ga), arsenic (4N, 6N and 7N) and germanium, pyrolitic boron nitride (pBN) crucibles for growing crystals, and boron oxide, these products are critical to the entire substrate manufacturing industry.

Cadmium telluride solar cell

A cadmium telluride solar cell is a solar cell based on cadmium telluride, an efficient light-absorbing material for thin-film cells. Compared to other thin-film materials, CdTe is easier to deposit and more suitable for large-scale production. There has been much discussion of the toxicity of CdTe-based solar cells. The perception of the toxicity of CdTe is based on the toxicity of elemental cadmium, a heavy metal that is a cumulative poison. While the toxicity of CdTe is presently under debate, it has been shown that the release of cadmium to the atmosphere is impossible during normal operation of the cells and is unlikely during fires in residential roofs. Furthermore, a square meter of CdTe contains approximately the

same amount of Cd as a single C cell Nickel-cadmium battery, in a more stable and less soluble form.

Copper indium gallium selenide solar cell

The materials based on $CuInSe_2$ that are of interest for photovoltaic applications include several elements from groups I, III and VI in the periodic table. These semiconductors are especially attractive for thin film solar cell application because of their high optical absorption coefficients and versatile optical and electrical characteristics which can in principle be manipulated and tuned for a specific need in a given device. CIS is an abbreviation for general chalcopyrite films of copper indium selenide (**CuInSe**$_2$), CIGS mentioned below is a variation of CIS. CIS films (no Ga) achieved greater than 14% efficiency. However, manufacturing costs of CIS solar cells at present are high when compared with amorphous silicon solar cells but continuing work is leading to more cost-effective production processes. The first large-scale production of CIS modules was started in 2006 in Germany by Würth Solar. Manufacturing techniques vary and include the use of Ultrasonic Nozzles for material deposition. Electro-Plating in other efficient technology to apply the CI(G)S layer. When gallium is substituted for some of the indium in CIS, the material is referred to as CIGS, or copper indium/gallium diselenide, a solid mixture of the semiconductors $CuInSe_2$ and $CuGaSe_2$, often abbreviated by the chemical formula $CuIn_xGa_{(1-x)}Se_2$. Unlike the conventional silicon based solar cell, which can be modelled as a simple p-n junction (see under semiconductor), these cells are best described by a more complex heterojunction model. The best efficiency of a thin-film solar cell as of March 2008 was 19.9% with CIGS absorber layer. Higher efficiencies (around 30%) can be obtained by using optics to concentrate the incident light or by using multi-junction tandem solar cells. The use of gallium increases the optical

bandgap of the CIGS layer as compared to pure CIS, thus increasing the open-circuit voltage, but decreasing the short circuit current. In another point of view, gallium is added to replace indium due to gallium's relative availability to indium. Approximately 70% of indium currently produced is used by the flat-screen monitor industry. However, the atomic ratio for Ga in the >19% efficient CIGS solar cells is ~7%, which corresponds to a bandgap of ~1.15 eV. CIGS solar cells with higher Ga amounts have lower efficiency. For example, CGS solar cells (which have a bandgap of ~1.7 eV have a record efficiency of 9.5% for pure CGS and 10.2% for surface-modified CGS. Some investors in solar technology worry that production of CIGS cells will be limited by the availability of indium. Producing 2 GW of CIGS cells (roughly the amount of silicon cells produced in 2006) would use about 10% of the indium produced in 2004. For comparison, silicon solar cells used up 33% of the world's electronic grade silicon production in 2006. Se allows for better uniformity across the layer and so the number of recombination sites in the film are reduced which benefits the quantum efficiency and thus the conversion efficiency.

Dye-sensitized solar cells

Typically a ruthenium metalorganic dye (Ru-centered) is used as a monolayer of light-absorbing material. The dye-sensitized solar cell depends on a mesoporous layer of nanoparticulate titanium dioxide to greatly amplify the surface area (200–300 m^2/g TiO_2, as compared to approximately 10 m^2/g of flat single crystal). The photogenerated electrons from the *light absorbing dye* are passed on to the *n-type* TiO_2, and the holes are passed to an electrolyte on the other side of the dye. The circuit is completed by a redox couple in the electrolyte, which can be liquid or solid. This type of cell allows a more flexible use of materials, and is typically manufactured by screen printing and/or use of Ultrasonic Nozzles, with the potential for lower processing costs than those used for *bulk* solar cells. However, the

dyes in these cells also suffer from degradation under heat and UV light, and the cell casing is difficult to seal due to the solvents used in assembly. In spite of the above, this is a popular emerging technology with some commercial impact forecast within this decade. The first commercial shipment of DSSC solar modules occurred in July 2009 from G24i Innovations

Organic/polymer solar cells

Organic solar cells and polymer solar cells are built from thin films (typically 100 nm) of organic semiconductors such as polymers and small-molecule compounds like polyphenylene vinylene, copper phthalocyanine (a blue or green organic pigment) and carbon fullerenes and fullerene derivatives such as PCBM. Energy conversion efficiencies achieved to date using conductive polymers are low compared to inorganic materials. However, it improved quickly in the last few years and the highest NREL (National Renewable Energy Laboratory) certified efficiency has reached 6.77%[42]. In addition, these cells could be beneficial for some applications where mechanical flexibility and disposability are important. These devices differ from inorganic semiconductor solar cells in that they do not rely on the large built-in electric field of a PN junction to separate the electrons and holes created when photons are absorbed. The active region of an organic device consists of two materials, one which acts as an electron donor and the other as an acceptor. When a photon is converted into an electron hole pair, typically in the donor material, the charges tend to remain bound in the form of an exciton, and are separated when the exciton diffuses to the donor-acceptor interface. The short exciton diffusion lengths of most

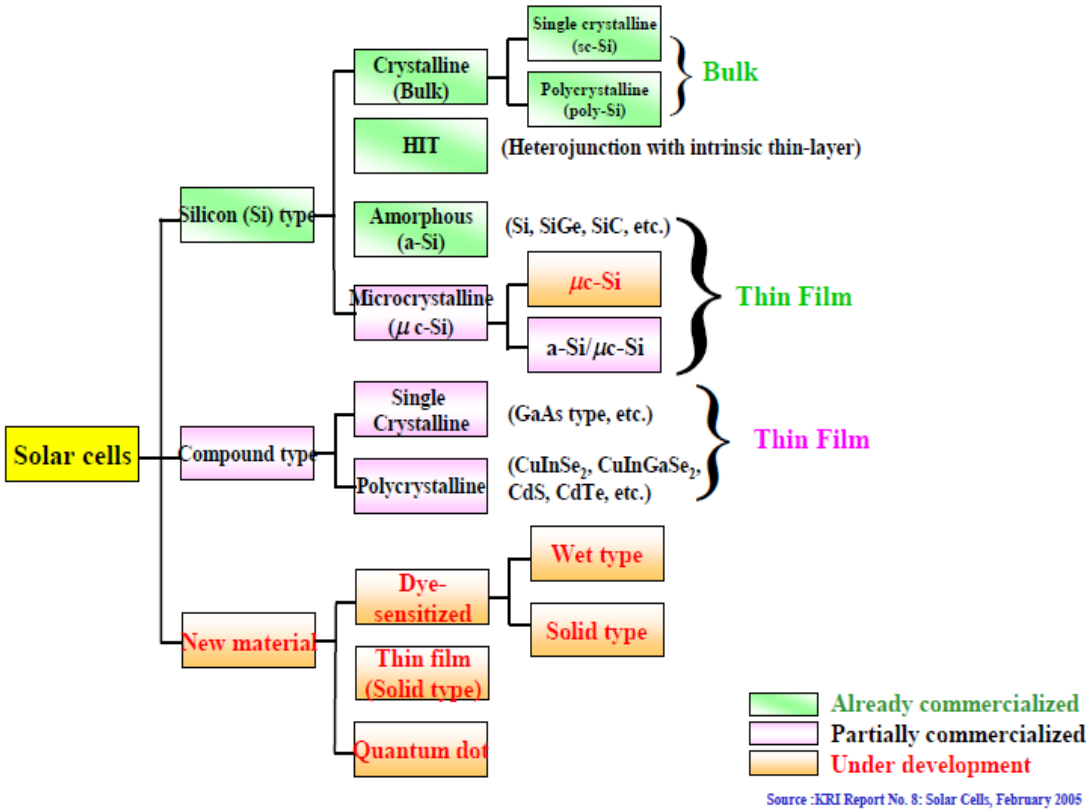

Figure 1 Category of Solar Cells

1.2 The Market of Solar Cell

In last section, it has introduced most kind of solar cells, including bulk silicon, thin film silicon, gallium arsenide multi-junction solar cell, CdTe, CIGS, and organic solar cells. But the mainstream of the market are still silicon base solar cells, which has already commercialized. The others are still under developed or partially commercialized. In recent years, the renewable energy has been taken more and more seriously and the demand of solar cells also increased significantly. The **figure 2** shows the production of solar cells in recent years. It indicates that the production significantly increases year by year and silicon based solar cells dominates the majority of market. In **figure 3**, it shows

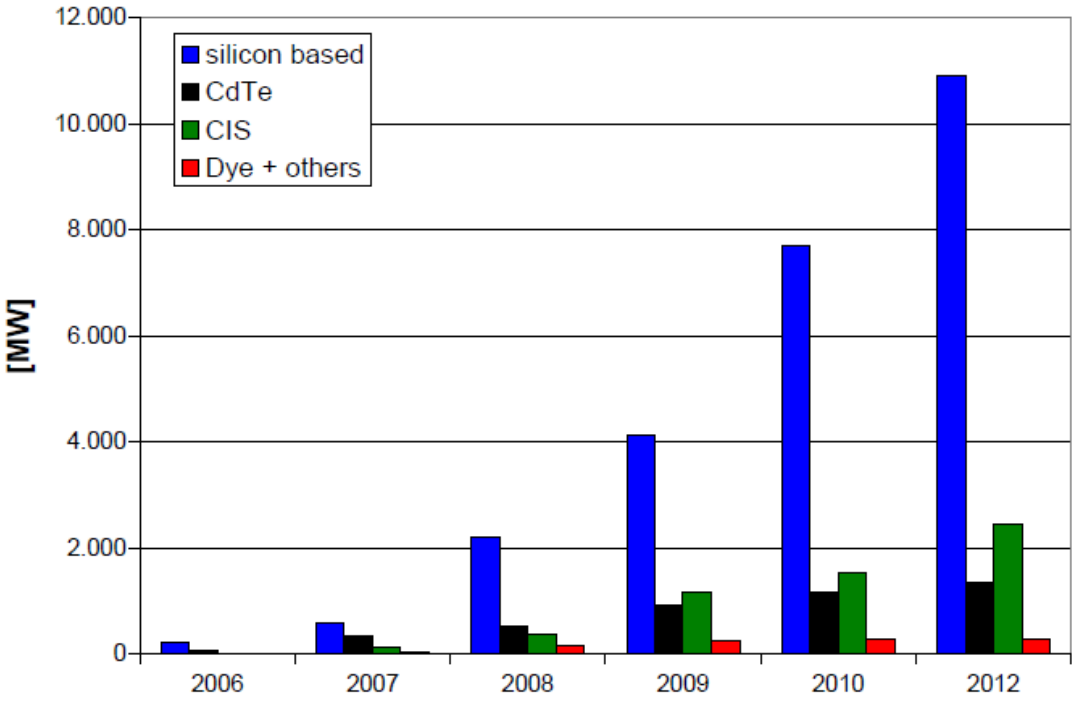

Figure 2 Comparison of Different Type of Solar Production

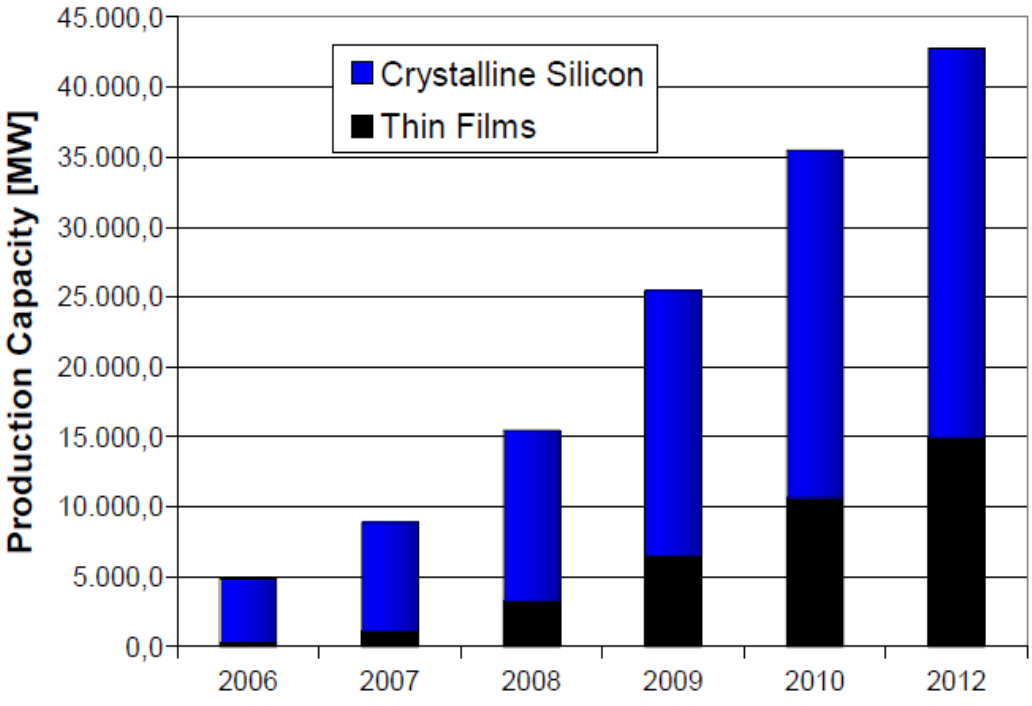

Figure 3 The Growth Trend of Thin Films and Crystalline Silicon Solar Cell over the Years

Chapter 2

Priciple of Semiconductor Solar Cells

Solar photovoltaic energy conversion is a one-step conversion process which generates electrical energy from light energy. The explanation relies on ideas from quantum theory. Light is made up of packets of energy, called photons, whose energy depends only upon the frequency, or color of the light The energy of visible photons is sufficient to exite electrons, bound into solids , up to higher energy levels where they are more free to move. An extreme example of this is photoelectric effect, the celebrated experiment which was explained by Einstein in 1905, where blue or ultraviolet light provides enough energy for electrons to escape completely from the surface of a metal. Normally, when light is absorbed by matter, photons are given up to excite electrons to higher energy states within the material, but the exited electrons quickly relax back to their ground state. In a photovoltaic device, howere, there is some built-in asymmetry which pulls the excited electrons away before they can relax, and feeds them to an external circuit. The extra motive force. This force drives the electrons through a load in the external circuit to do electrical work. The effectiveness of a photovoltaic device depends on the choice of light absorbing materials and the way in which they are connected to the external circuit. In this chapter I will summarize the characteristics and discuss its physical function in detail.

2.1 Solar Radiation

The radiative energy output from the sun derives from a nuclear fusion reaction. In every second about 6x 10^{11} kg of H, is converted to He, with a net mass loss of about 4x10^{3} kg, which is converted through the Einstein relation ($E = mc^2$) to 4x 10^{20} J. This energy is emitted primarily as electromagnetic radiation in the ultraviolet to infrared and radio spectral ranges (0.2 to 3 um). The total mass of the sun is now about 2x10^{30} kg, and a reasonably stable life

with a nearly constant radiative energy output over 10 billion (10^{10}) years is projected. The intensity of solar radiation in free space at the average distance of the earth from the sun has a value of 1,353 W/m^2. The atmosphere attenuates the sunlight when it reaches the earth's surface, mainly due to water-vapor absorption in the infrared, ozone absorption in the ultraviolet, and scattering by airborne dust and aerosols. The degree to which the atmosphere affects the sunlight received at the earth's surface is quantified by the air mass. The secant of the angle between the sun and the zenith is defined as the air mass (AM) number and it measures the atmospheric path length relative to the minimum path length when the sun is directly overhead. The AM0 thus represents the solar spectrum outside the earth's atmosphere. The AM1 spectrum represents the sunlight at the earth's surface when the sun is at zenith (sec(x)), see **Figure 4**, and the incident power is about 925 W/m^2. The AM2 spectrum is for x=60^o and has an incident power of about 691 W/m2, and so on. **Figure 5** shows the solar spectrums at various AM conditions. The upper curve is the AM0 condition which can be approximated by a 5,800 K black-body radiation, as shown by the dashed curve. The AM0 spectrum is the relevant one for satellite and space-vehicle applications. The AM1.5 conditions (with sun at x=45^o above the horizon) represent a satisfactory energy-weighted average for terrestrial applications. For solar-cell energy conversion, each photon produces an electron-hole pair, so the solar power has to be converted to photon flux. The photon flux density per unit energy for AM1.5 is shown in **Fig. 6** together with wavelength to photon energy. The total incident power for AM 1.5 is 844 W/m^2[1].

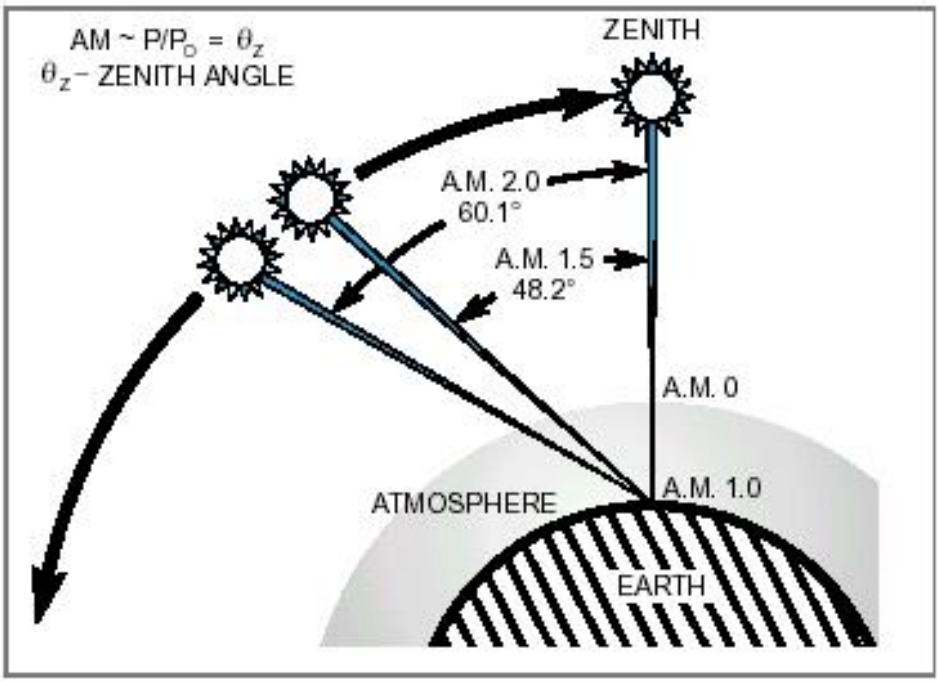

Figure 4 The Zenith Angle of the Sun

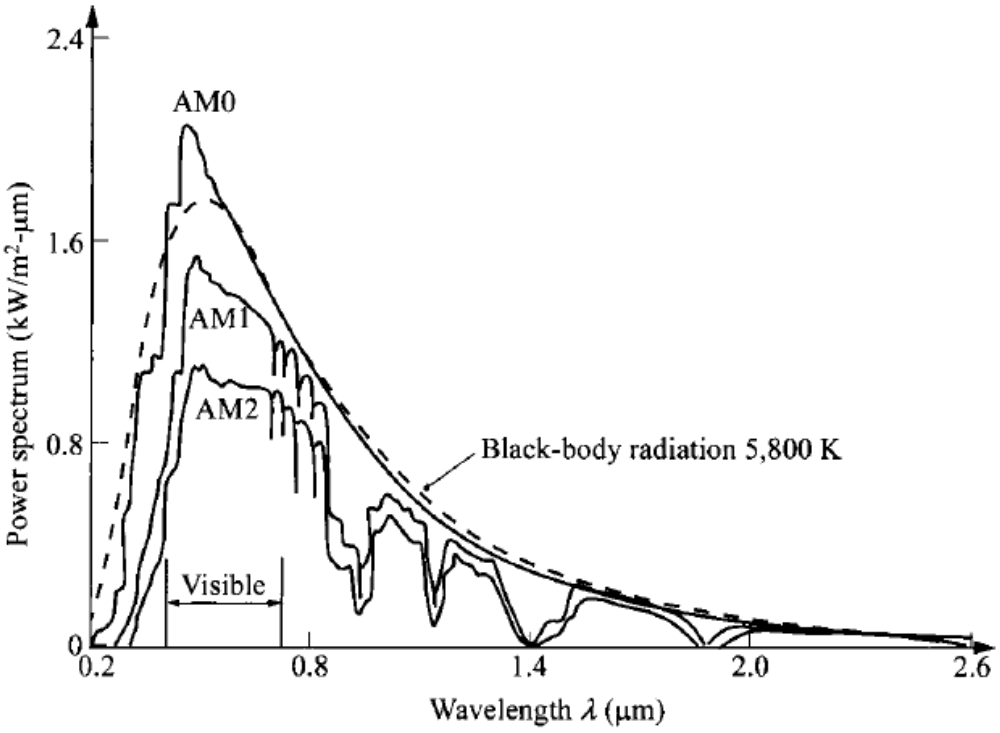

Figure 5 Solar Spectrum at Different Air-Mass Conditions

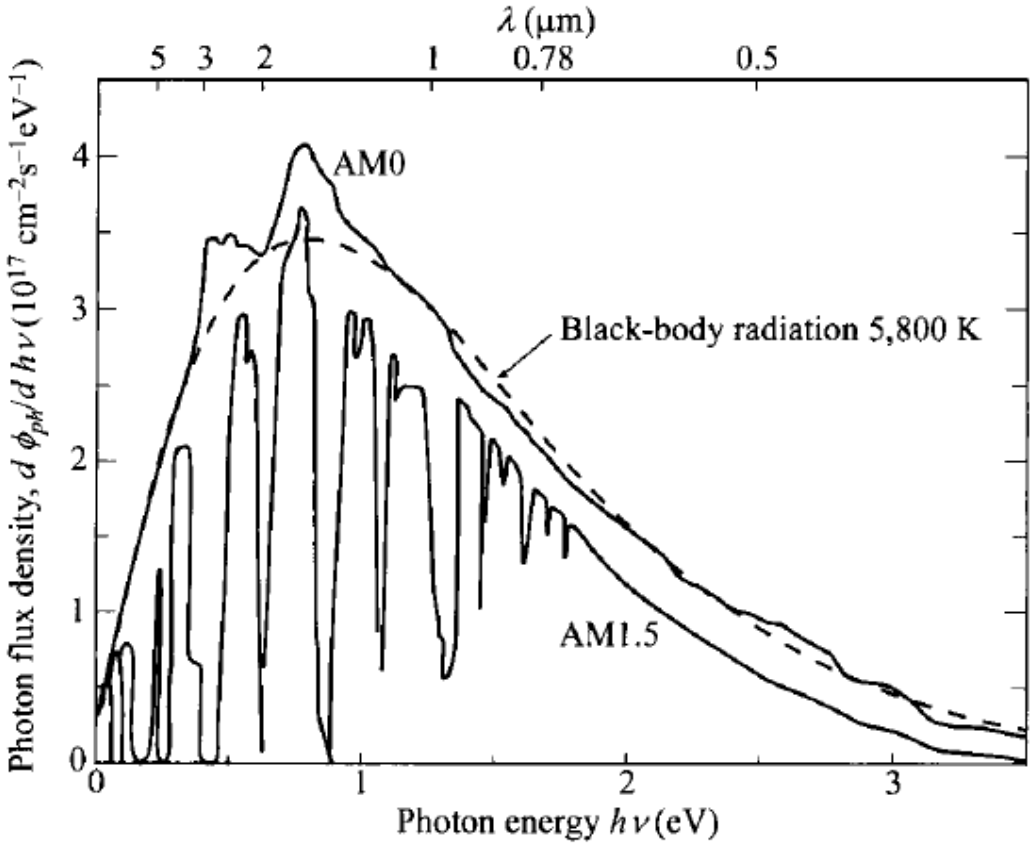

Figure 6 Solar Spectrum in Photon Flux Density per Photon Energy for AM0 and AM1.5 Conditions[2]

2.2 PN Junction in Equilibrium

A solar cell is a pn junction device with no voltage directly applied across the junction. The solar cell converts photon power into electrical power and delivers this power to a load. In this section, I will introduce the primary characteristics of pn junction in equilibrium. **Figure 7** schematically shows the pn junction. One region is doped with acceptor impurity atoms to form the p region and the adjacent region is doped with donor atoms to form the n region. Majority carrier electrons in the n region will begin diffusing into the p region and majority carrier holes in the p region will begin diffusing into the n region. If we assume there are no external connections to the semiconductor, then this diffusion process cannot continue indefinitely. As electrons diffuse from the n region, positively charged donor atoms are left behind. Similarly, as holes diffuse from the p region, they uncover negatively charged

acceptor atoms. The net positive and negative charges in the n and p regions induce an electric field in the region near the metallurgical junction, in the direction from the positive to the negative charge, or from the n to the p region[3].

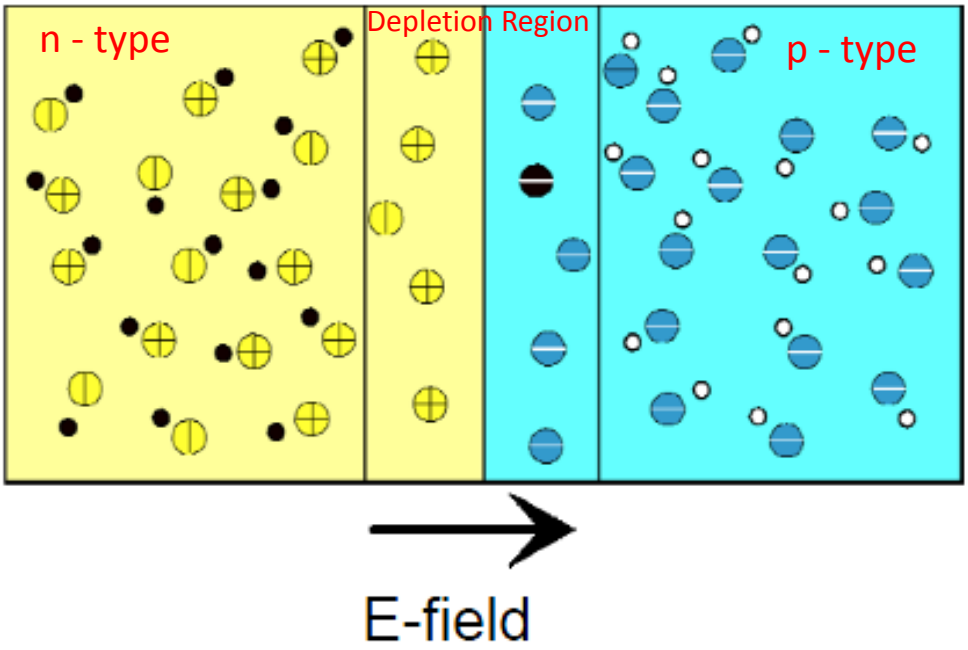

Figure 7 The electric field and forces acting on the charged carrier in the space charge region

If we assume that no voltage is applied across the pn junction, then the junction is in thermal equilibrium which means the Fermi energy level is constant throughout the entire system. **Figure 8** shows the energy-band diagram for the pn junction in thermal equilibrium. The conduction and valance band energies must bend as we go through the space charge region, since the relative position of the conduction and valence bands with respect to the Fermi energy changes between p and n regions. This potential barrier is referred to as the built-in potential barrier and is denoted by

$$q\psi_0 = E_G - E_{Fn} - E_{Fp} = kT\ln\left(\frac{N_A N_D}{n_i^2}\right) \qquad E_{Fn} = kT\ln(N_C/N_D) \qquad E_{Fp} = kT\ln(N_V/N_A) \tag{1}$$

The built-in potential barrier maintains equilibrium between majority carrier electrons in the n region and minority carrier electrons in the p region, and also between majority carrier holes

in the p region and minority carrier holes in the n region. The potential barrier maintains equilibrium, so no current is produced by this voltage.

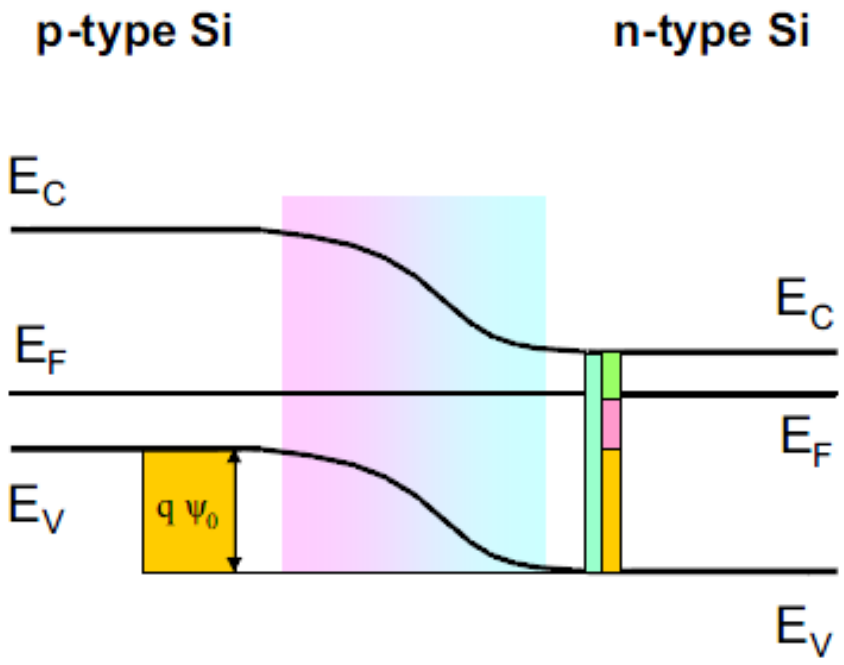

Figure 8 Energy band diagram of a pn junction in thermal equilibrium

In t he depletion region consists of a region of fixed charge corresponding to the ionized dopant atoms cores that lost their carriers due to the diffusion current. The depletion region tails off exponentially away from the junction edge. Assuming that the depletion region is zero a certain distance away from the junction edge (called the depletion region width) greatly simplified analysis. Above assumption is called depletion region approximation: the depletion approximation assumes that the electric field is confined to a finite region. For constant doping it approximates the charge density as constant in the transition region, and zero everywhere else. The amount of charge on the two sides of the depletion region must be equal. The width of the depletion region can be calculated by integrating the charge density in the depletion region to get the electric field, and then integrating again to get an expression for the built-on voltage, whose value we already know from the difference in the Fermi levels.

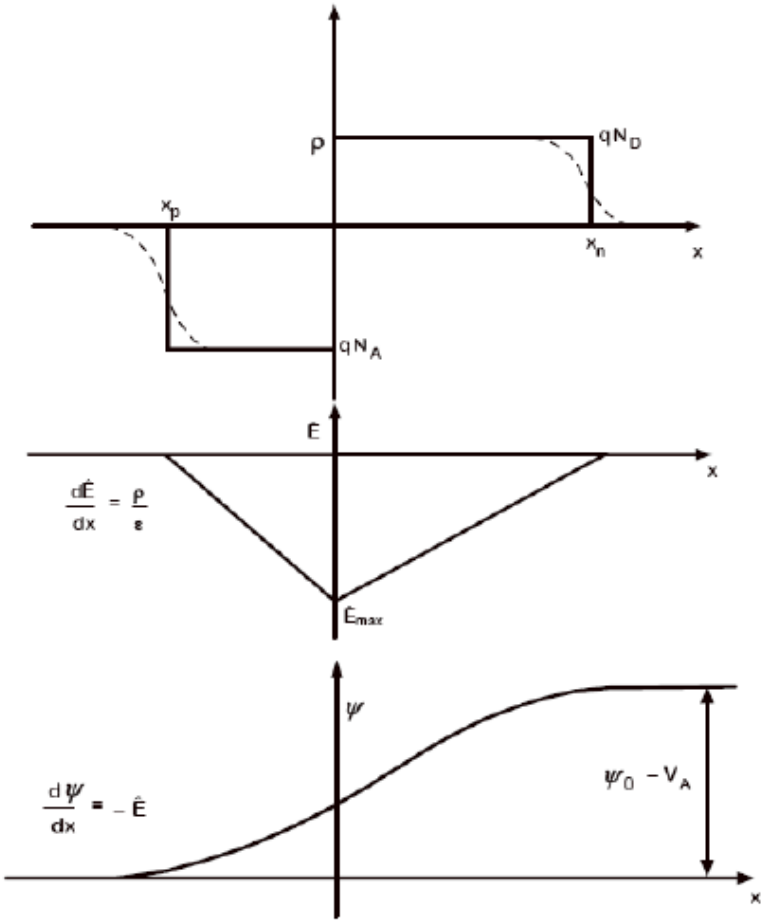

Figure 9 The space charge density, electric field, and electric field potential through the space charge region of a uniformly doped pn junction

$$\frac{d\hat{E}}{dx} = \rho \qquad \rho = \begin{cases} -\dfrac{qN_A}{\varepsilon_s} & when\ x_p \le x < 0 \\ \dfrac{qN_D}{\varepsilon_s} & when\ 0 \le x < x_n \end{cases} \qquad N_A x_p = N_D x_n \tag{2}$$

Integrating twice and stting this equal to the built in voltage, allows us to find the maximum value of the electric field.

$$\hat{\mathbf{E}}_{\mathbf{max}} = -\left[2.\, \mathbf{e} \Big/ \boldsymbol{\varepsilon}_s \left(\frac{\boldsymbol{\Psi}_0}{\dfrac{1}{\mathbf{N_A}} + \dfrac{1}{\mathbf{N_D}}} \right) \right]^{1/2} \tag{3}$$

The depletion region width is given by:

$$W = X_p + X_n = \left[2.{}^{\varepsilon_s}\!/_{e} \left((\Psi_0).\left(\frac{1}{N_A} + \frac{1}{N_D} \right) \right) \right]^{1/2}$$

$$X_p = W.\frac{N_D}{N_D + N_A} \qquad X_n = W.\frac{N_A}{N_D + N_A} \qquad (4)$$

The maximum electric field increases as the doping increases and is controlled by the doping of the more lightly doped side. The depletion region width is also controlled by the more lightly doped side.

Ideal pn Junction Current

The total current in the junction is the sum of the individual electron and hole currents which are constant through the depletion region. Since the electron and hole currents are continuous functions through the pn junction, the total pn junction current will be the minority carrier hole diffusion current at $x=x_n$ plus the minority carrier electron diffusion current at $x=x_p$ The gradients in the minority carrier concentrations, as shown in **Figure 10**, produce diffusion currents, and since we are assuming the electric field to be zero at the space charge edges, we can neglect any minority carrier drift current component.

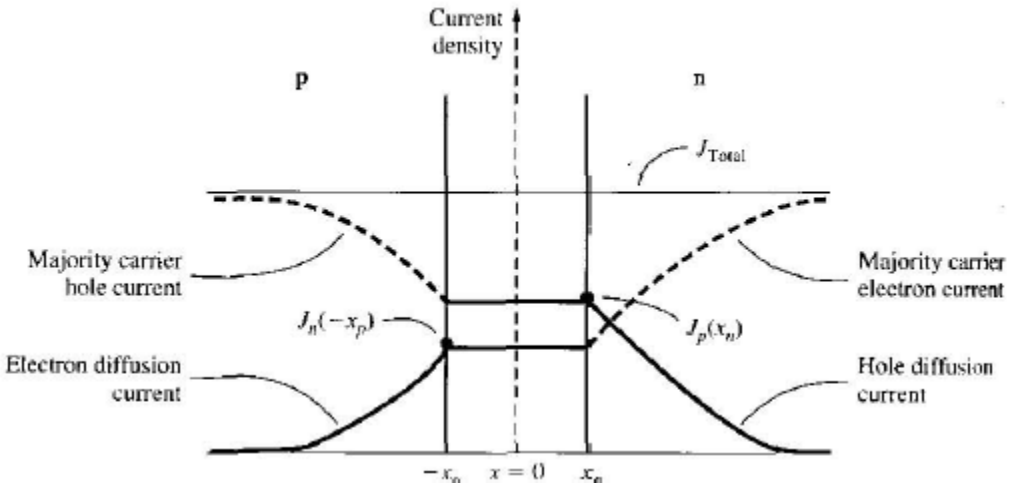

Figure 10 Minority carrier concentrations in a pn junction under forward bias.

We calculated the minority carrier diffusion current densities at the edge of the space charge region. We can determine the minority carrier diffusion current densities as a function of distance through p and n regions. These results are

$$J_p(x) = \frac{eD_p p_{n0}}{L_p}\left[\exp\left(\frac{eV_a}{kT}\right) - 1\right]\exp\left(\frac{x_n - x}{L_p}\right)$$

$$J_n(x) = \frac{eD_n n_{p0}}{L_n}\left[\exp\left(\frac{eV_a}{kT}\right) - 1\right]\exp\left(\frac{x_p + x}{L_n}\right) \quad (5)$$

The total current density in the pn junction is then

$$J = J_p(x_n) + J_n(-x_p) = \left[\frac{eD_p p_{n0}}{L_p} + \frac{eD_n n_{p0}}{L_n}\right]\left[\exp\left(\frac{eV_a}{kT}\right) - 1\right] \quad (6)$$

We define a parameter Js as

$$J_s = \left[\frac{eD_p p_{n0}}{L_p} + \frac{eD_n n_{p0}}{L_n}\right] \quad (7)$$

So that, the ideal current-voltage equation of pn junction, see **Figure 11**, can be written as

$$J \simeq J_s\left[\exp\left(\frac{eV_a}{kT}\right) - 1\right] \quad (8)$$

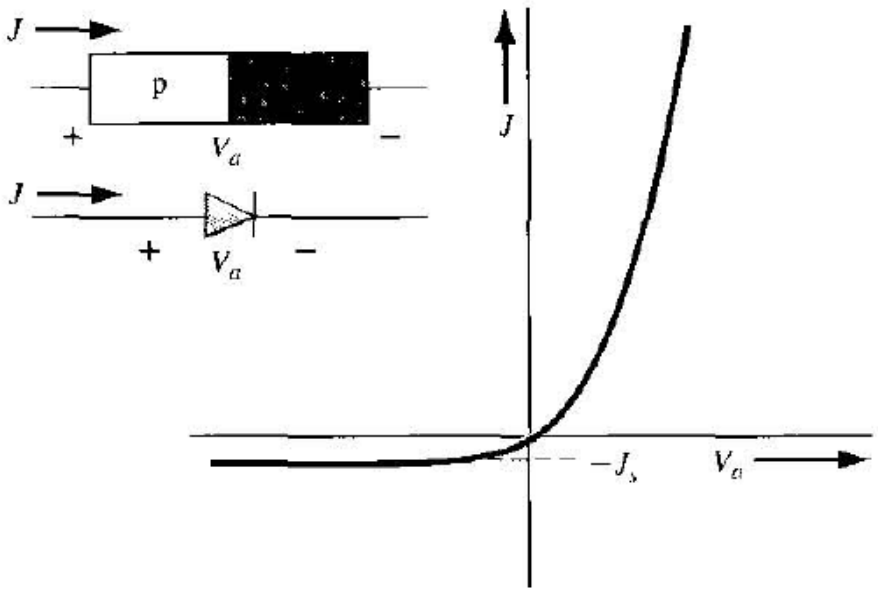

Figure 11 Ideal I-V characteristic of a pn junction diode.

2.3 Under Illumination

Solar cell is based on the photovoltaic effect. As a cell is under illumination, absorption of light leads to generate electron-hole pairs. **Figure 12** shows that light with different wavelength would be absorbed at the different depth. Then, the charged carriers would be separated by the electric field in depletion region. At last, the electrode collects the carriers.

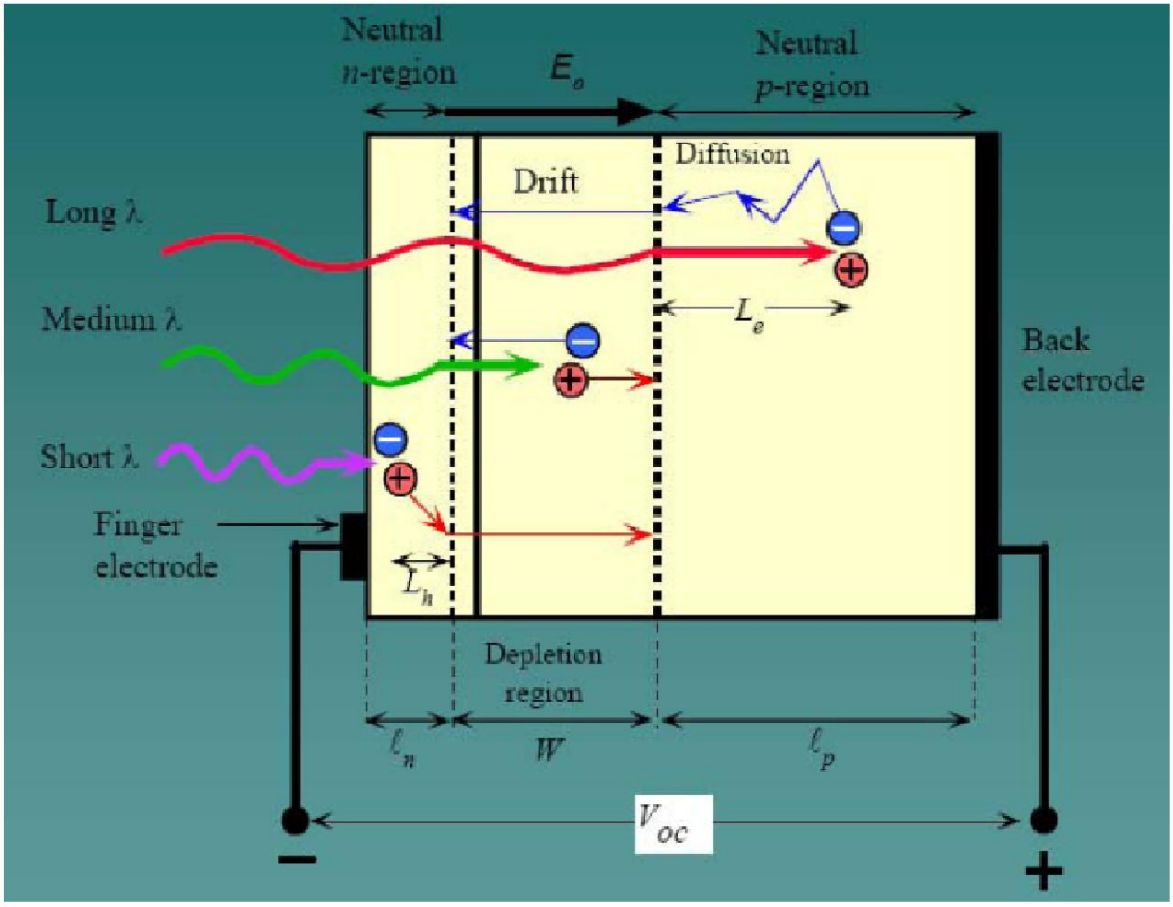

Figure 12 Operation of Solar Cell

Con sider the pn junction with a resitive load. Even with zero bias applied to the junction, an electric field exists in the space charge region. Incident photon illumination can create electron-hole pairs in the space charge region that will be swept out p producing the photocurrent I_L in the reverse-bias direction. The photo current I_L produces a boltage drop across the resitive load which forward biases the pn junction. The forward-bias voltage produces a forward-bias current. The net pn junction current, in the reverse-bias direction, is

$$I = I_L - I_s(e^{V/V_T} - 1) \tag{9}$$

Where the ideal diode equation has been used. **Figure 13** shows the equivalent circuit of pn solar cell, where I is output current density, and V is output voltage on the load. As the diode becomes forward biased the magnitude of the electric field in the space charge region decreases, but does not go to zero or change direction. The photocurrent is always in the reverse-bias direction and the net solar cell current is also always in the reverse-bias direction. There are two limiting cases of interest. The short-circuit condition occurs when R_{load}=0 so that V=0. The current in this case is referred to as the short-circuit current, or

$$I = I_{SC} = I_L \tag{10}$$

The second limiting case is the open-circuit condition and occurs when $R_{load} \rightarrow \infty$. The net current is zero and the voltage produced is the open-circuit voltage. The photocurrent is just balanced by the forward –biased junction current so we have

$$I = 0 = I_L - I_s(e^{Voc/V_T} - 1) \tag{11}$$

We can find the open circuit voltage V_{oc} as

$$V = V_{OC} = V_T \ln\left(\frac{I_L}{I_S} + 1\right) \tag{12}$$

A plot of the diode current I as a function of the diode voltage V from the above equation is shown in **Figure 14**. We may note the short-circuit current and open –circuit voltage points on the figure.

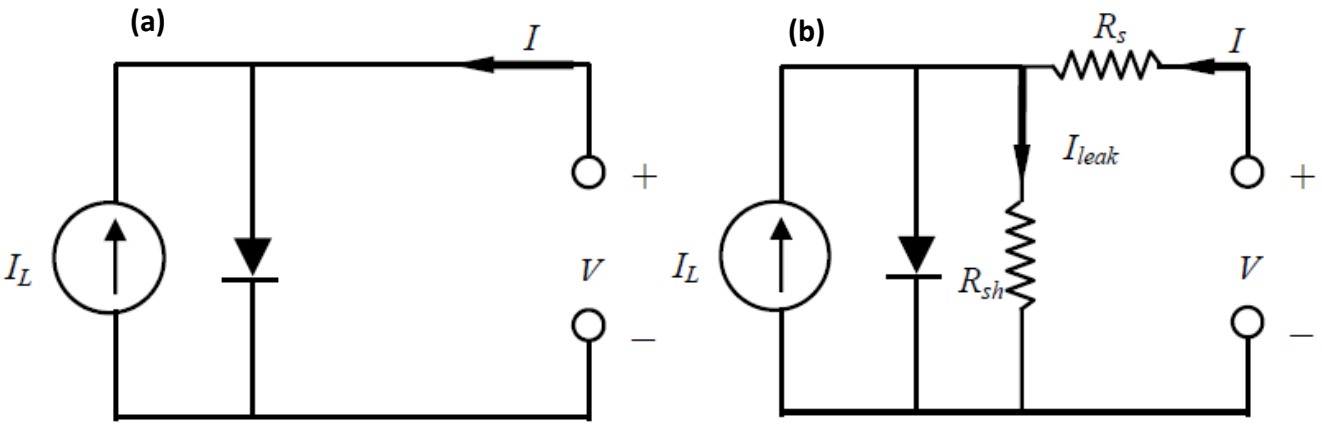

Figure 13 Equivalent Circuit of pn Solar Cell (a) without (b) with parallel and series resistance

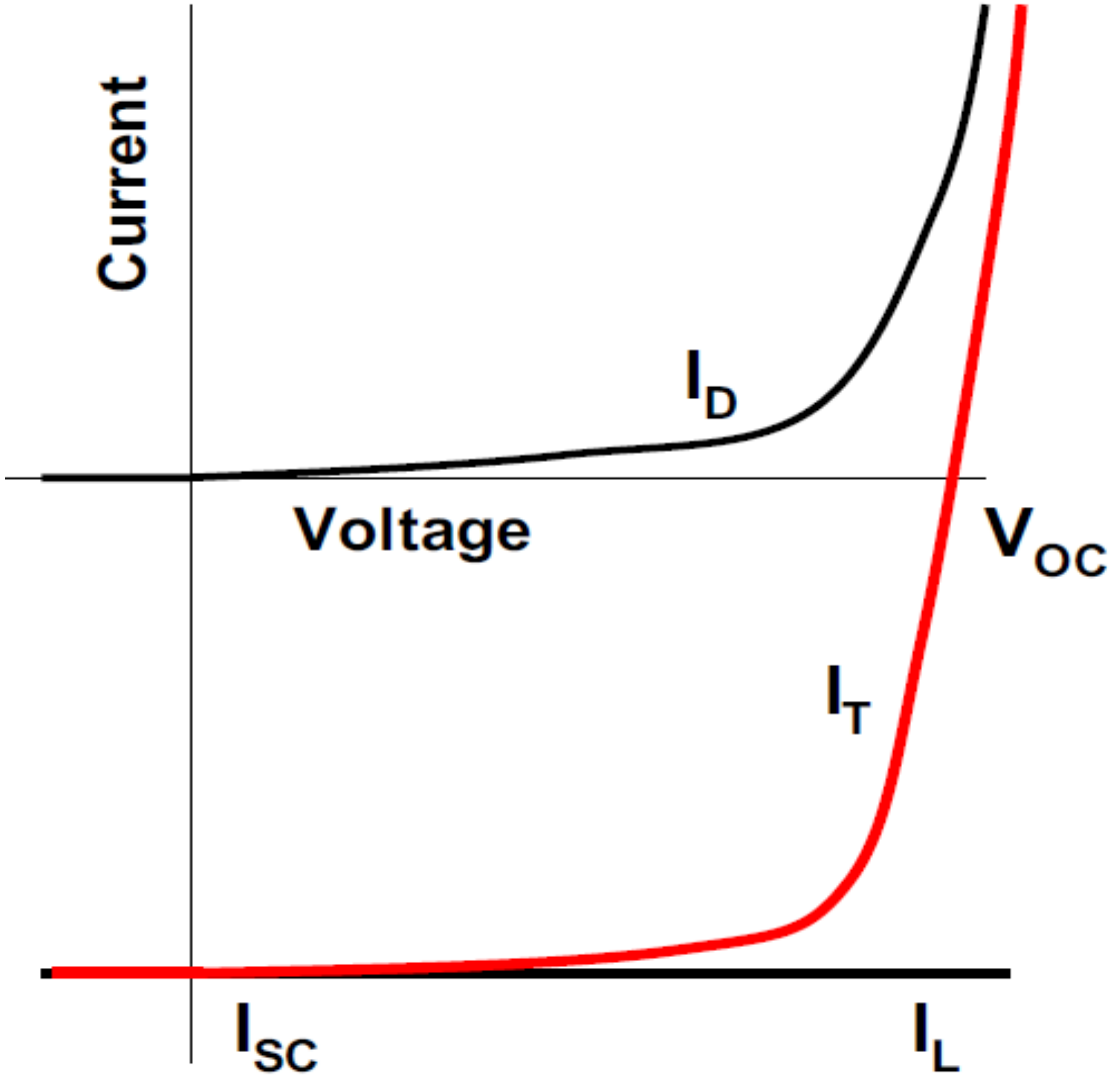

Figure 14 Illuminated I-V Characteristic

The power delivers on the load is

$$P = IV = I_S V(e^{V/V_T} - 1) - I_L V \tag{13}$$

We may find the current and voltage which will deliver the maximum power to the load by setting the derivative equal to zero. We find

$$V_{P\max} = V_T \ln\left(\frac{I_L / I_S + 1}{V_{P\max} / V_T + 1}\right) \tag{14}$$

$$I_{P\max} = I_S \frac{V_{P\max}}{V_T} e^{V_{P\max}/V_T} \tag{15}$$

$$P_{\max} = I_{P\max} V_{P\max} \tag{16}$$

The conversion efficiency of a solar cell is defined as the ration of output electrical power to incident optical power. For the maximum power output, we can write

$$\eta = \frac{P_{\max}}{P_{in}} \times 100\% \tag{17}$$

The maximum possible current and the maximum possible voltage in the solar cell are I_{sc} and V_{oc}, respectively. The ration $I_m V_m / I_{sc} V_{oc}$ is called the fill factor and is a measure of the realizable power from a solar cell. Typically, the fill factor is between 0.6 to 0.8.

$$FF \equiv \frac{P_{\max}}{I_{SC} V_{OC}} \tag{18}$$

The conversion efficiency can be also written as

$$\eta = \frac{FF \cdot I_{SC} \cdot V_{OC}}{P_{in}} \tag{19}$$

In real cells power is dissipated through the resistance of the contacts and through leakage currents around the sides of the device. These effects are equivalent electrically to two parasitic resistances in series Rs and in parallel Rsh with the cell, see **Figure 13(b)**. The series resistance arises from the resistance of the cell material to current flow, particularly through the front surface to the contacts, and from resistive contacts. Series resistance is a particular problem at high current densities, for instance under concentrated light. The parallel or shunt resistance arises from leakage of current through the cell, around the edges of the device and between contacts of different polarity. It is a problem in poorly rectifying devices. Series and parallel resistances reduce the fill factor as shown in **Figure 15** For an efficient cell we want Rs to be as small and Rsh to be as large as possible. When parasitic resistances are included, the diode equation becomes

$$I = I_L - I_S\left[e^{(V-IR_S)/V_T} - 1\right] - \frac{V - IR_S}{R_{sh}} \tag{20}$$

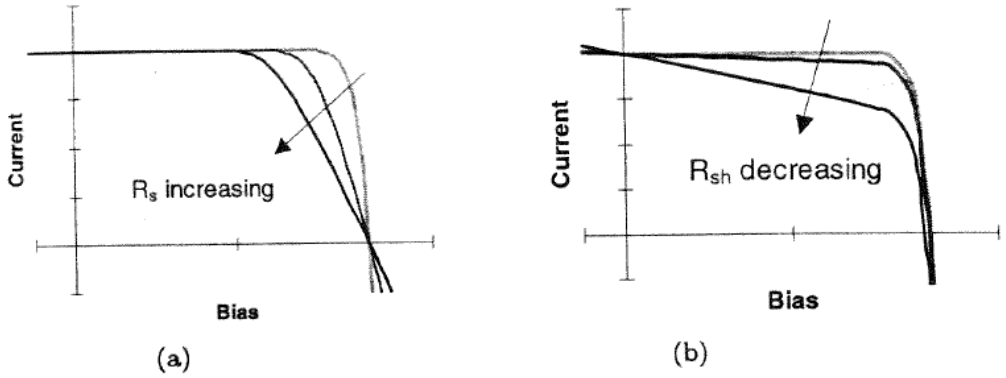

Figure 15 Effect of (a) incrising series and (b) reducing parallel resistances. In each case the outer curve has

Rs=0 .and Rsh=∞

Chapter 3

Experiment Instrument & Measurement System

In this chapter, I would introduce you our experiment instrument and measurement system we use in NDL. We use high density plasma chemical vapor deposition system(HDPCVD), E-gun evaporator deposition system and DC magnetrons sputter deposition system to fabricate thin film solar cell. Then, we use N&K measurement system and UV-Visible transmission spectrum system to measure the reflection rate, transmission rate, refractive index and absorption coefficient. At last, I will introduce how we measure the characteristic, including conversion efficiency and quantum efficiency of solar cell.

3.1 High Density Plasma Chemical Vapor Deposition System

We use high density plasma chemical vapor deposition system to fabricate amorphous or microcrystalline silicon thin film. High density plasma system has high fractional ionization capacity. The high dissociation capacity of HDPCVD can be used to yield high-density plasma and markedly increased electron temperature, promoting the diffusion capability of the reactive radicals and eventually yielding low-defect a-Si and microcrystalline Si (μc-Si) films at low temperatures. Unlike PECVD, the electrode of high density plasma chemical vapor deposition system is a coil of flat metal like a spiral, see **Figure 16.** The energy is supplied by electrical currents which are produced by electromagnetic induction, that is, by time-varying magnetic fields. It ionized the reactive gases and produce glow discharge which lead to faster deposition rate. In the high density plasma chemical vapor deposition system, the reactive energy is from not thermal energy but inductively coupled plasma, so the temperature of the substrates is just about 100~300^{o}C, which is one of its advantage.

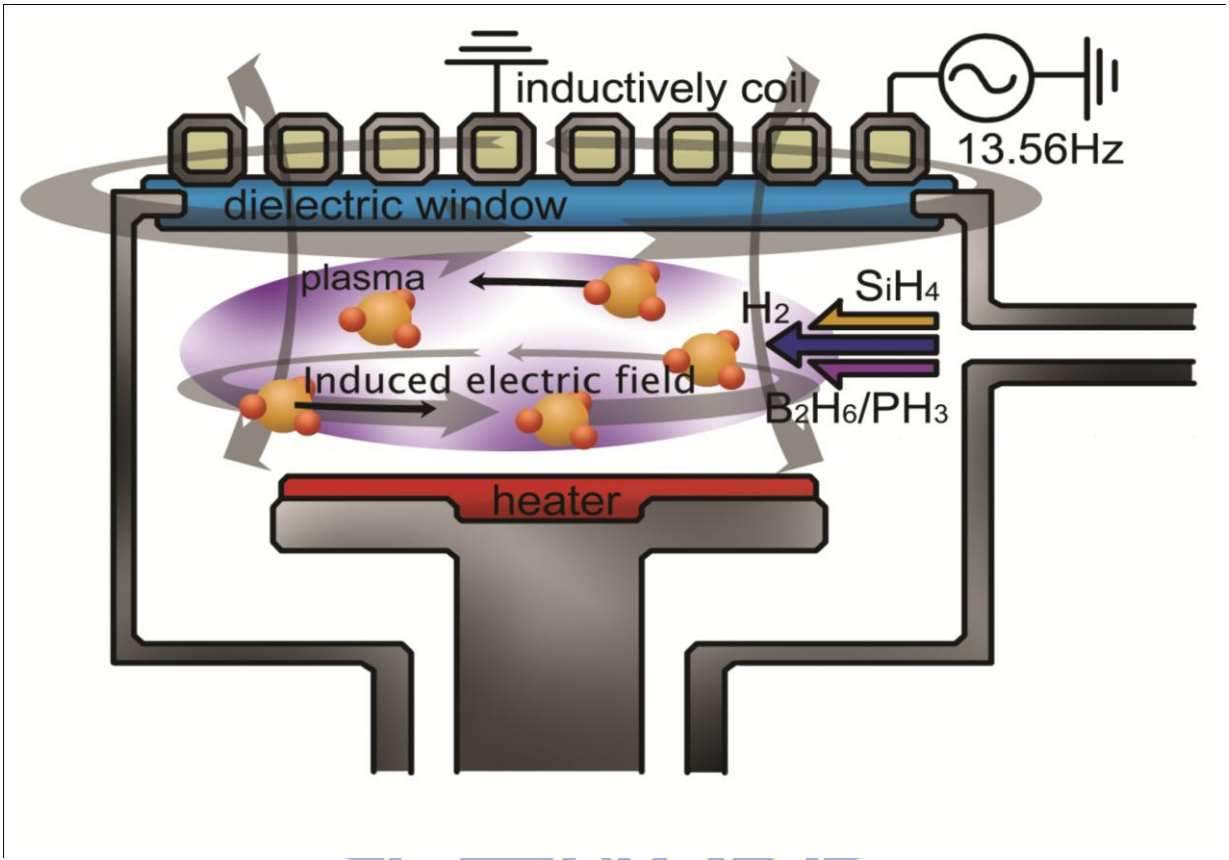

Figure 16 The High Density Plasma Chemical Vapor Deposition System

3.2 E-Gun Evaporator Deposition System

An E-gun evaporator fires a high-energy beam from an electron gun to boil a small spot of material; since the heating is not uniform, lower vapor pressure materials can be deposited. The beam is usually bent through an angle of 270° in order to ensure that the gun filament is not directly exposed to the evaporant flux, see **Figure 17.** We can use the system to fabricate metal gate on our devices. The metal material includes Al, Ni and Ag. The base pressure and process pressure is 5E-7 torr and 8E-6 respectively.Typical deposition rates for E-gun evaporation range from 5 to 100 angstrom per second.

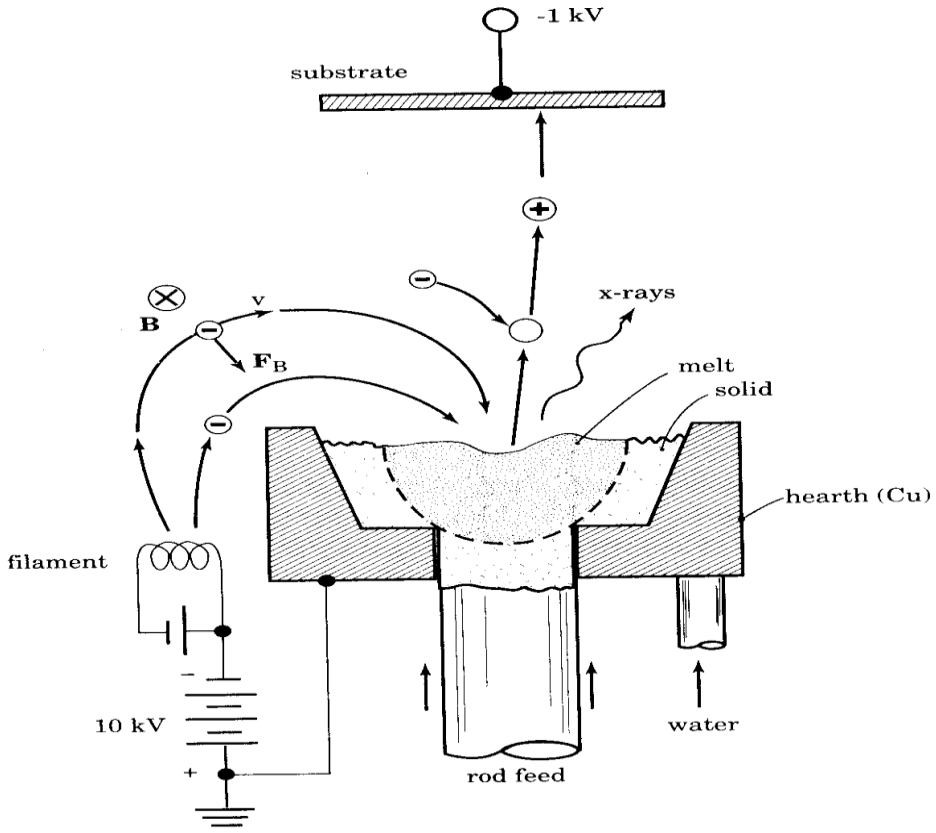

Figure 17 E-gun Evaporator Deposition System

3.3 DC Magnetrons Sputter Deposition

Sputter deposition is a physical vapor deposition (PVD) method of depositing thin films by sputtering, that is ejecting, material from a "target," that is source, which then deposits onto a substrate, such as a silicon wafer. Sputtered atoms ejected from the target have a wide energy distribution, typically up to tens of eV (100000 K). The sputtered ions (typically only a small fraction — order 1% — of the ejected particles are ionized) can ballistically fly from the target in straight lines and impact energetically on the substrates or vacuum chamber (causing resputtering). Alternatively, at higher gas pressures, the ions collide with the gas atoms that act as a moderator and move diffusively, reaching the substrates or vacuum chamber wall and condensing after undergoing a random walk. The entire range from high-energy ballistic impact to low-energy thermalized motion is accessible by changing the background gas pressure. The sputtering gas is often an inert gas such as argon. For efficient momentum

transfer, the atomic weight of the sputtering gas should be close to the atomic weight of the target, so for sputtering light elements neon is preferable, while for heavy elements krypton or xenon are used. Reactive gases can also be used to sputter compounds. The compound can be formed on the target surface, in-flight or on the substrate depending on the process parameters. The availability of many parameters that control sputter deposition make it a complex process, but also allow experts a large degree of control over the growth and microstructure of the film.

3.4 N&K Analyzer

The system simultaneously determines film thickness, n and k in the spectral range of 190 to 1000 nm, and provides non-destructive, real time, high throughput measurements directly on the device. The n&k system is also equipped with an automated X-Y stage for full sample mapping.

3.5 UV-Visible Spectroscopy

The UV-Visible spectroscopy system could measure the absorption and transmission of the material in the range of 200~1000 nm. The ultraviolet and visible spectroscopy uses light in the visible and adjacent (near-UV and near-infrared (NIR)) ranges. The absorption in the visible range directly affects the perceived color of the chemicals involved. In this region of the electromagnetic spectrum, molecules undergo electronic transitions. This technique is complementary to fluorescence spectroscopy, in that fluorescence deals with transitions from the excited state to the ground state, while absorption measures transitions from the ground state to the excited state.

3.6 Solar Simulator

The solar simulator we use is Sol3A Class AAA Solar Simulator, type No. 94063A made by Newport. Sol3A Class AAA Solar Simulator with a 1000 Watt Xenon source and 6 x 6 inch illuminated area. All Oriel Sol3A simulators are certified to IEC 60904-9 Edition 2 (2007), JIS C 8912, and ASTM E 927-05 standards for Spectral Match, Non-Uniformity of Irradiance, and Temporal Instability of Irradiance. The Oriel Sol3A simulators all use a single lamp design to meet not one or two, but all three performance criteria without compromising the 1 Sun output power, providing true Class AAA performance. The system uses a black non-reflective finish to minimize stray light and incorporates captive screws for all panels requiring user access to facilitate lamp replacement, alignment, and filter changes. Safety interlocks prevent inadvertent exposure to UV light.

After we fabricate the Si thin film solar cell, we use the light from solar simulator illuminate on the device which connects to Keithley 2440 to make a I-V measurement, see **Figure 18**. Because of the incident light illuminates on the side of glass, we have to overturn the device and the Al electrode faces down. Then, we need a probe station which have the flip function, see **Figure 19.**

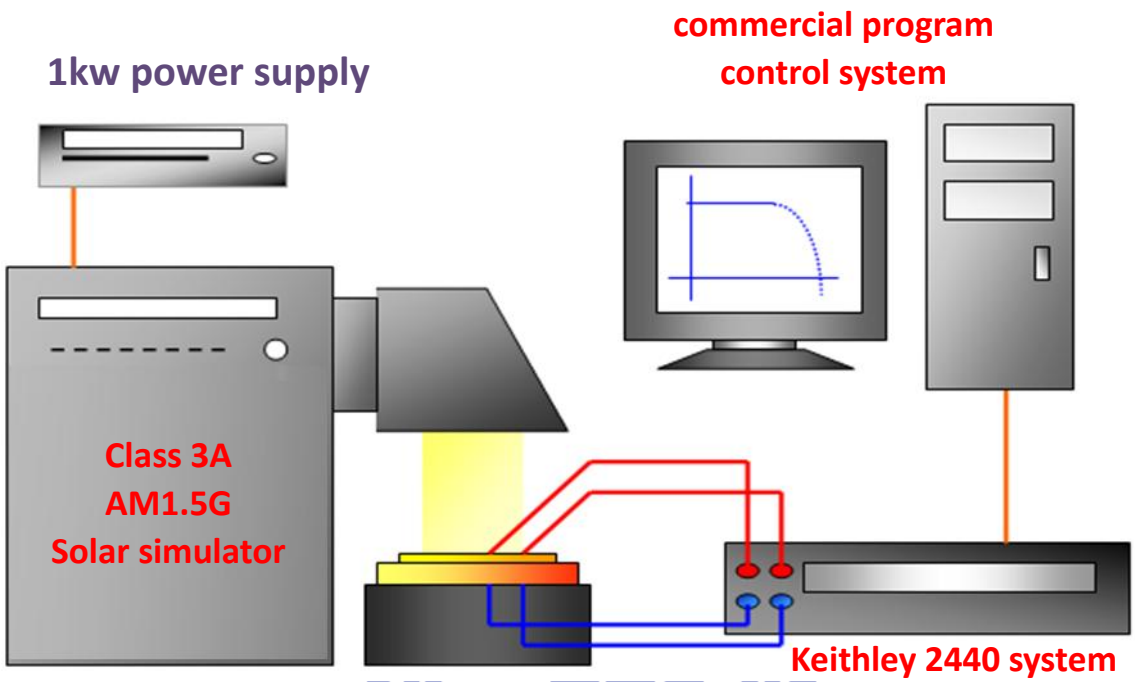

Figure 18 Solar Simulator System and I-V Measurement

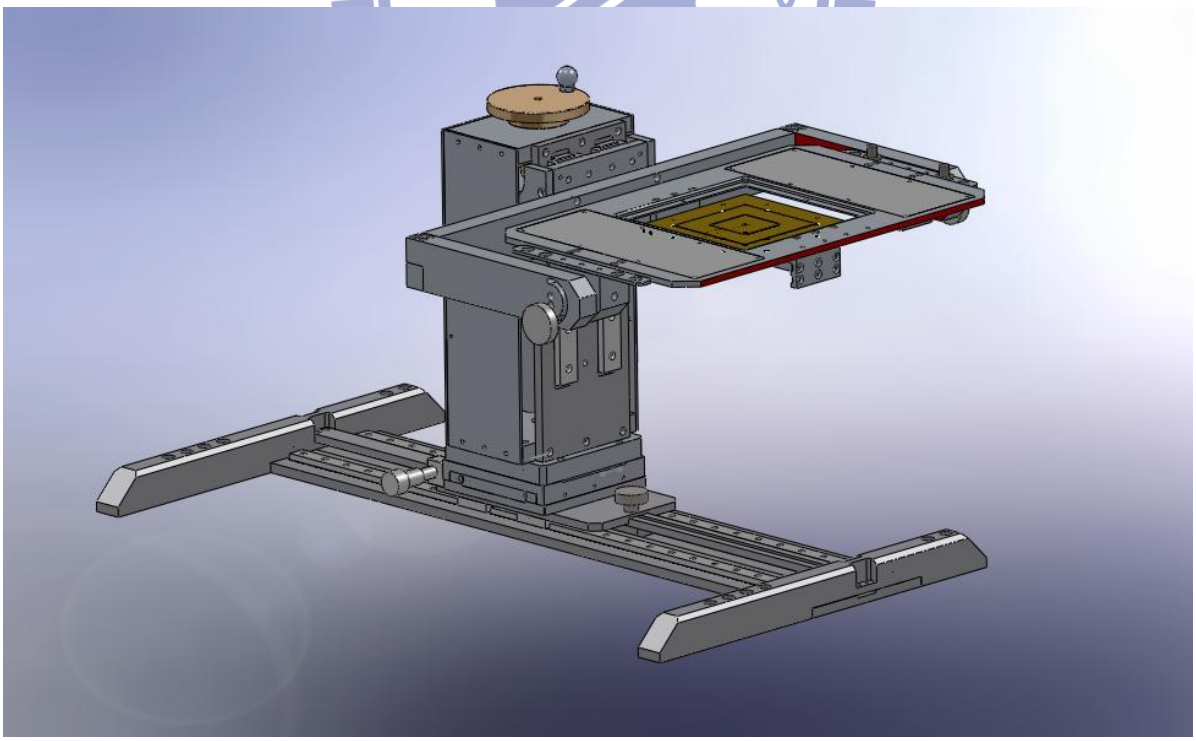

Figure 19 Probe Station with Flip Function

3.7 QE Measurement

Quantum efficiency (QE) is a quantity defined for a solar cell as the percentage of photons hitting the photoreactive surface that will produce an electron–hole pair. It is an accurate measurement of the device's electrical sensitivity to light. Since the energy of a photon depends on (more precisely, is inversely proportional to) its wavelength, QE is often measured over a range of different wavelengths to characterize a device's efficiency at each photon energy. Solar cell typically has a QE about 10~90%, while solar cell can have a QE of well over 90% at some wavelengths. The quantum efficiency of a solar cell is a very important measure for solar cells as it gives information on the current that a given cell will produce when illuminated by a particular wavelength. If the quantum efficiency is integrated (summed) over the whole solar electromagnetic spectrum, one can evaluate the current that a cell will produce when exposed to the solar spectrum. The ratio between this current and the highest possible current (if the QE was 100% over the whole spectrum) gives the electrical efficiency of the solar cell. With solar cells, one often measures the external quantum efficiency (EQE, sometimes also simply referred to as QE), which is the current obtained outside the device per incoming photon.

$$\mathrm{EQE} = \frac{\text{electrons/sec}}{\text{photons/sec}} = \frac{\text{current/(charge of 1 electron)}}{\text{(total power of photons)/(energy of one photon)}}$$

The external quantum efficiency therefore depends on both the absorption of light and the collection of charges. Once a photon has been absorbed and has generated an electron-hole pair, these charges must be separated and collected at the junction. A "good" material avoids charge recombination and therefore a drop in the external quantum efficiency.

Chapter 4

Device Fabrication Process and Growth Mechanism

4.1 Device Fabrication Process

In our experiment, we use HDP-CVD deposition system to fabricate silicon thin film solar cell. The gas we use includes silane(SiH_4), hydrogen(H_2), argon(Ar), phosphine(PH_3), and Diborane (B_2H_6). The followings show the fabrication process in our experiment.

I. System Inspection:

At first, we would check if the pump, gas flow, heater operate normally, and if the pressure as low as we want (lower than 5.0E-5mTorr)

II. Chamber Clean:

We should clean the chamber before we deposit amorphous silicon thin film. First of all, open the valve and inflow CF_4, O_2 and Ar into the chamber. The flow rate of CF_4, O_2, Ar is 200sccm, 100sccm, 50sccm respectively which are controlled by MFC(Mass Flow Controller). As the pressure in the chamber is 100mtorr, start the RF power, set the power as 500w which could ionize CF_4 in to plasma. The plasma can do dry etching on the chamber.

III. Place Holder:

Vent the load lock, place the holder into chamber by robot arm.

IV. Pre-Deposition:

As the pressure is low enough(lower than 5.0E10-5Torr), the valve would open and the MFC would control the gas flow. After the pressure we set is stable. RF power starts and it would do pre-deposition 10 min.

V. Film Deposition:

Put the substrate we use on the holder and place the holder into chamber, then we can start to do film deposition.

VI. Process Finish:

Take the substrate out from the chamber, inflow the N_2 to vent the load lock

Process Flowchart

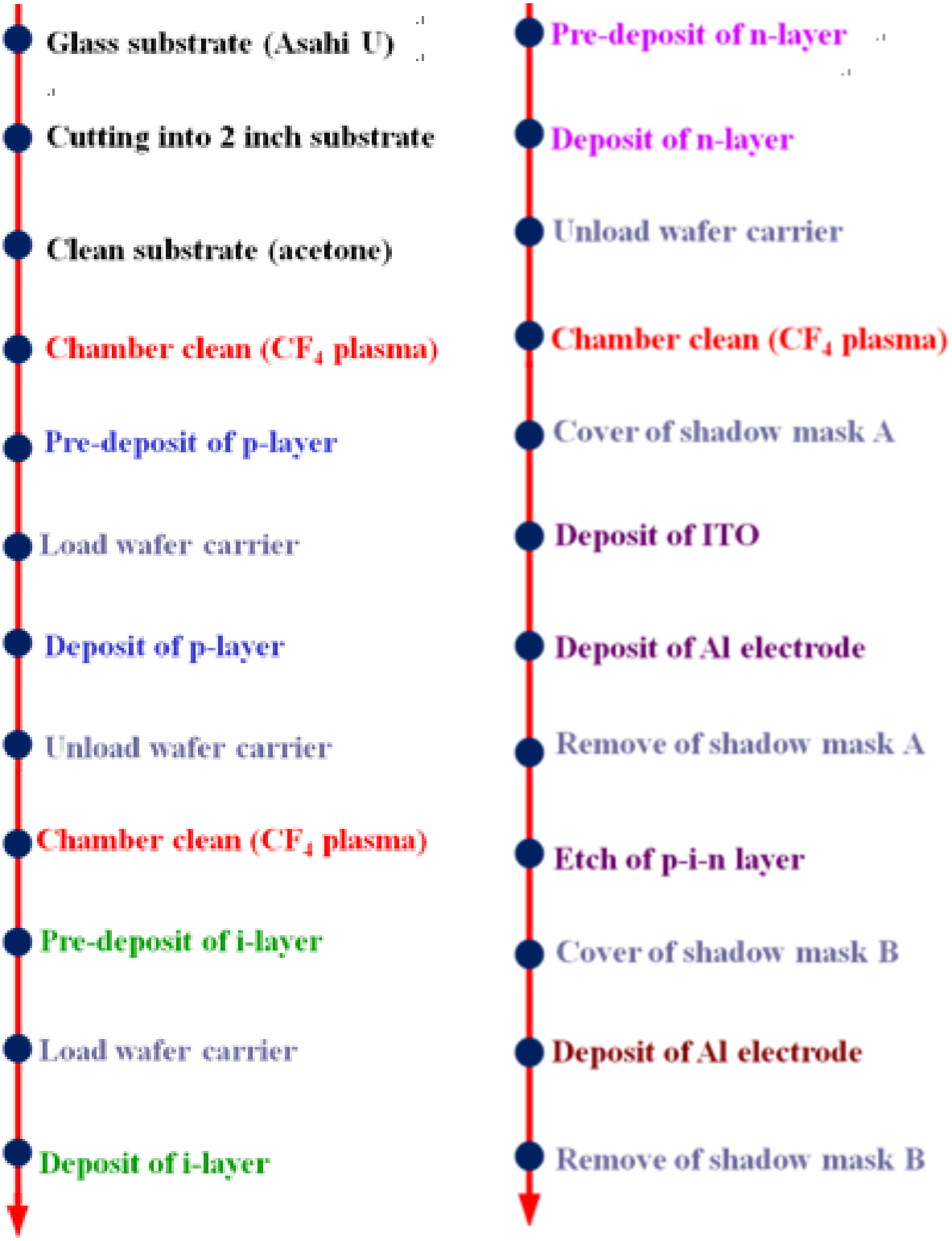

4.2 Thin Film Growth Mechanism

a-Si has been used as a photovoltaic solar cell material for calculators for some time. Although they are lower performance than traditional c-Si solar cells, this is not important in calculators, which use very low power. a-Si's ability to be easily deposited during construction more than makes up for any downsides. More recently, improvements in a-Si construction techniques have made them more attractive for large-area solar cell use as well. Here their lower inherent efficiency is made up, at least partially, by their thinness - higher efficiencies can be reached by stacking several thin-film cells on top of each other, each one tuned to work well at a specific frequency of light. This approach is not applicable to c-Si cells, which are thick as a result of their construction technique and are therefore largely opaque, blocking light from reaching other layers in a stack. The main advantage of a-Si in large scale production is not efficiency, but cost. a-Si cells use approximately 1% of the silicon needed for typical c-Si cells, and the cost of the silicon is by far the largest factor in cell cost. However, the higher costs of manufacture due to the multi-layer construction have, to date, make a-Si unattractive except in roles where their thinness or flexibility are an advantage.

Chapter 5

Experiment Result and Discussion

5.1 Thin Film Analysis

In this section, I will introduce you the growth condition of each layers fabricated by HDPCVD and its material structure and optical properties.

5.1.1 The Growth Condition of Each Layers Fabricated by HDPCVD

There are many reason affect the film quality, such as base pressure, process pressure, RF power, flow rate of gas, and temperature of substrate. The reasons above would influence film's quality and structure, including defect density, absorption, refractive index. In order to fabricate hydrogenated silicon thin film solar cell, we should dope diborane and phosphine to obtain p-layer and n-layer respectively, and I also doped the GeH_4 to deposit amorphous silicon germanium alloy thin film. The followings are the detailed deposition conditions of intrinsic layer, p-layer, n-layer and a-SiGe layer.

I. p-layer :

Substrate temperature: 150~250^{o}C, RF power : 10 to 50W, process pressure : 500~1500mtorr, SiH_4 : 5~20sccm, H_2 : 100~500sccm, B_2H_6/SiH_4 : 1~10%, deposition rate : 0.5~3 Å /s

II. i-layer:

Substrate temperature: 150~250^{o}C, RF power : 10 to 50W, process pressure : 500~1500mtorr, SiH_4 : 5~20sccm, H_2 : 100~500sccm, deposition rate : 0.8~2.5 Å /s

III. n-layer:

Substrate temperature: 150~250^{o}C, RF power : 10 to 50W, process pressure : 500~1500mtorr, SiH_4 : 5~20sccm, H_2 : 100~500sccm, PH_3/SiH_4 : 1~5%, deposition rate : 0.5~3 Å /s

IV. a-SiGe:

V. Substrate temperature: 150~250°C, RF power : 10 to 50W, process pressure : 500~1500mtorr, SiH_4 : 5~20sccm, H_2 : 100~500sccm, GeH_4/SiH_4 : 1~20%, deposition rate : 1~1.8 Å /s

5.1.2 Material Structure and Optical Characteristic

The N&K Analyzer can measure the refractive index, n and extinction coefficient, k. The extinction coefficient is refers to several different measures of the absorption of light in a medium. In physics, the "extinction coefficient" is the imaginary part of the complex index of refraction, which also relates to light absorption. **Figure 20** shows the typical n&k of a-Si:H with different SiH_4/H_2 ratio [4]. It shows that the refractive index and extinction coefficient vary with different SiH_4/H_2 ratio.

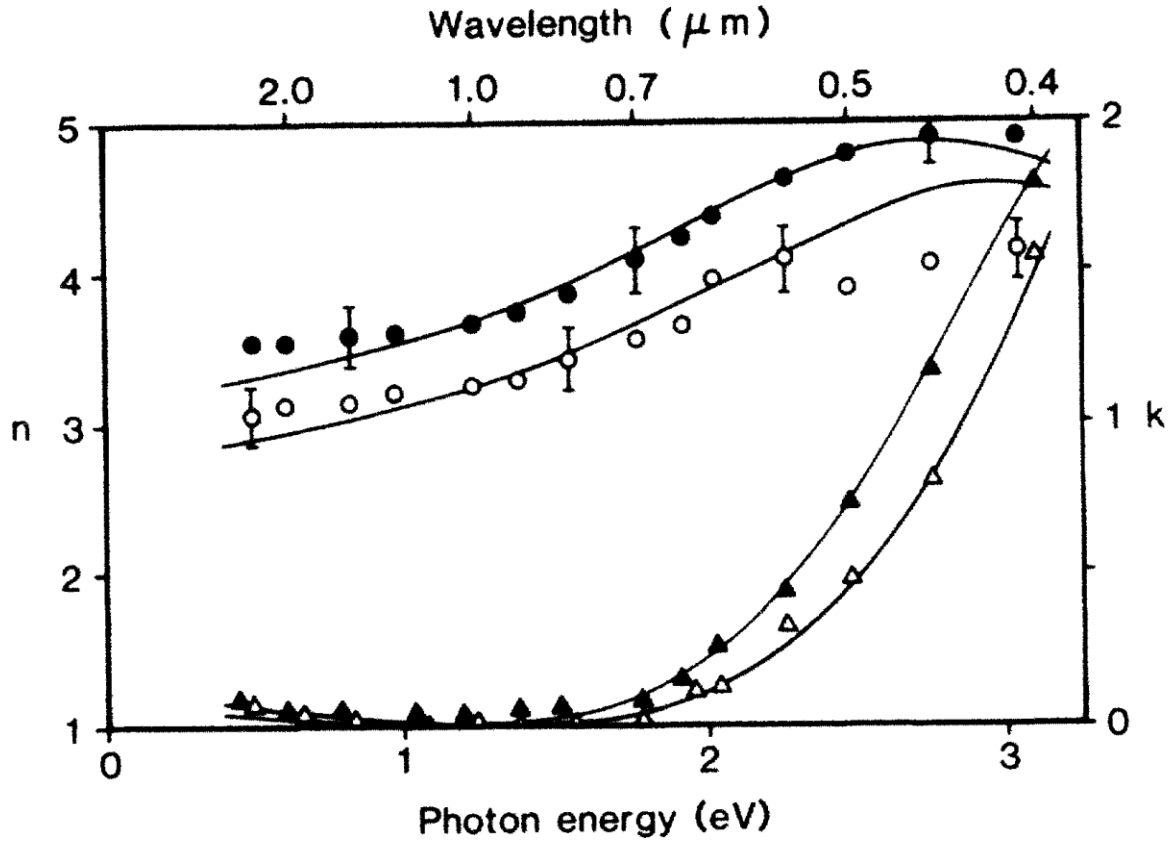

Figure 20 typical a-Si:H n&K corresponds to wavelength and photon energy

The **Table 1** shows the most typical parameter and refractive index of p-layer, i-layer and

n-layer in our experiment. And the **Figure 21~23** show the n&k of each layer.

Layer	SiH_4/H_2 (sccm)	Ar (sccm)	Dopant/SiH_4 (%)	Refractive Index (633nm)	Deposition rate (A/sec)
p-layer	10/200	200	10	4.07	3.63
i-layer	15/150	100	-	3.9	1.43
n-layer	10/200	200	5	3.97	1.53

Table 1. The parameter and refractive index of p-layer, i-layer and n-layer in our experiment.

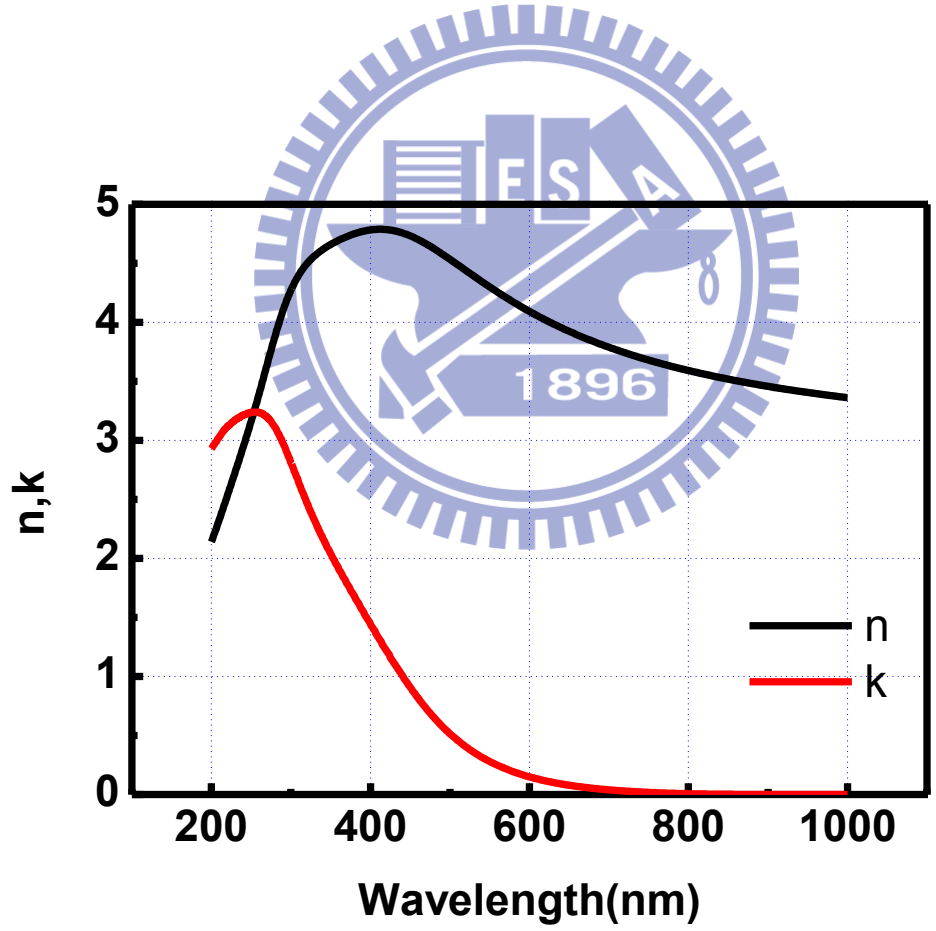

Figure 21 Refractive Index and Extinction Coefficient of p-layer Corresponds to Wavelength

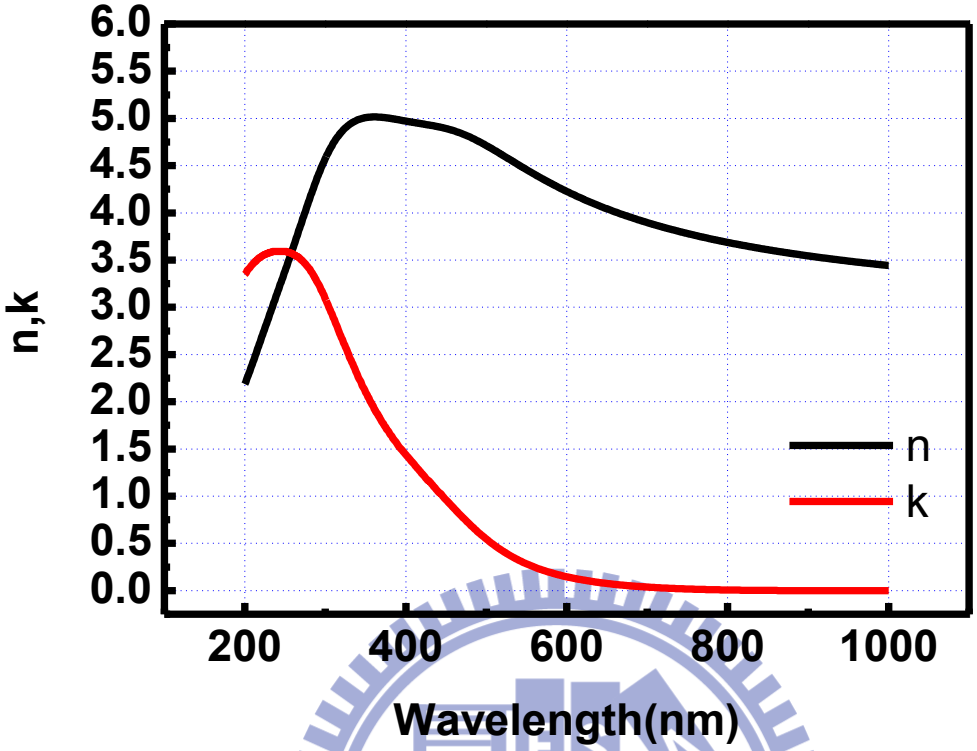

Figure 22 Refractive Index and Extinction Coefficient of i-layer Corresponds to Wavelength

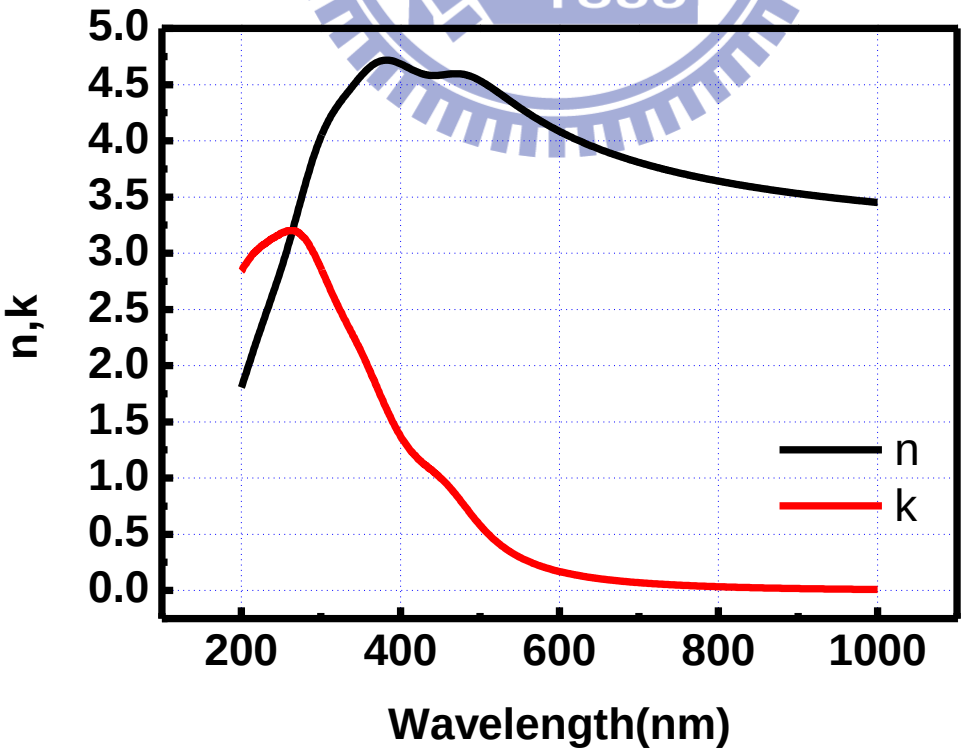

Figure 23 Refractive Index and Extinction Coefficient of n-layer Corresponds to Wavelength

The relation between extinction coefficient and material absorption coefficient is

$$\alpha = \frac{4\pi k}{\lambda} \tag{16}$$

In order to obtain the optical band gap of each layer in our amorphous silicon thin film solar cell, I would substitute the extinction coefficient into Tauc model[5]. Tauc model is used to determine the optical gap, or Tauc gap, in amorphous thin film materials. The Tauc gap is often used to characterize practical optical properties of amorphous materials. The formula to obtain Tauc gap is

$$(\alpha h\upsilon)^{1/2} \sim c(h\upsilon - E_g) \tag{17}$$

Where α is absorption coefficient, h is Plank constant, υ is the light frequency and E_g is the optical bandgap. The resulting plot has a distinct linear regime which denotes the onset of absorption. Thus, extrapolating this linear region to the abscissa yields the energy of the optical band gap of the material. Generally, the optical bandgap of amorphous silicon is between 1.75~1.9 eV. The Tauc plot with linear extrapolation to determine the Tauc optical gap for each layers are 1.90eV, 1.89eV, and 1.91eV respectively, which are shown in **Figure 24~26**. The results mean that the optical band gap of each layers are large enough to absorb long wavelength region in visible solar spectra. According the above result, we can use this method to obtain the optical band gap. In this paper, our ultimate purpose is to use silicon alloy with carbon and germanium to engineer the optical bandgap, which can effectively utilize the broadband solar spectra. The **table 2 and Figure 27~38** shows that if we inflow more GeH_4, we could obtain the lower optical bandgap. Then, we can use the intrinsic SiGe films to fabricate amorphous silicon germanium single junction solar cell and a-Si/a-SiGe tandem solar cell.

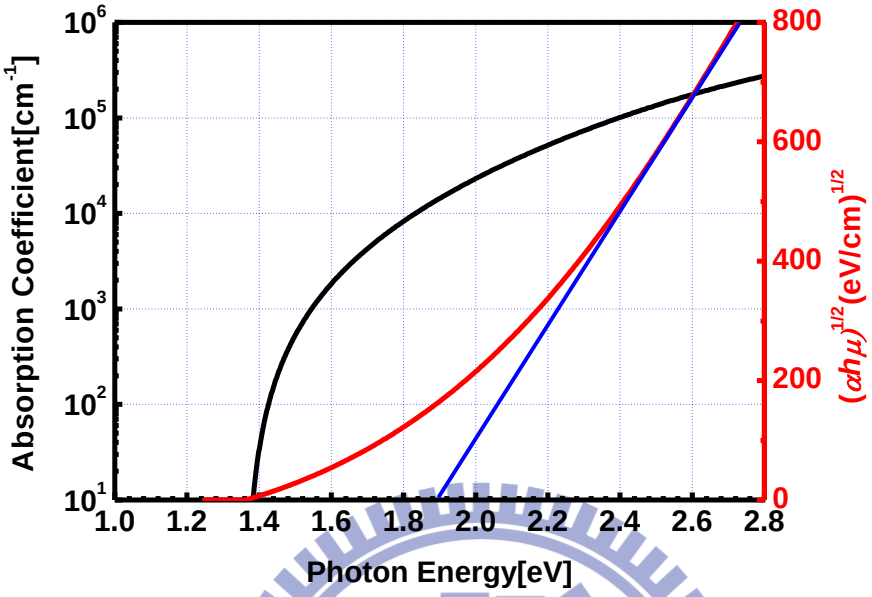

Figure 24 P-layer Absorption Coefficient Corresponds to the Photon Energy and Optical band gap fitting by Tauc Plot

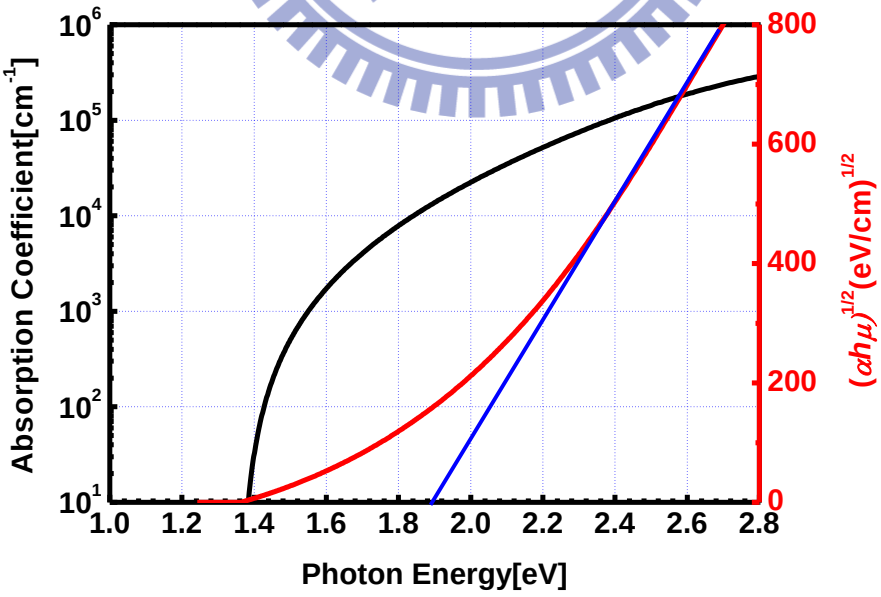

Figure 25 I-layer Absorption Coefficient Corresponds to the Photon Energy and Optical band gap fitting by

Tauc Plot

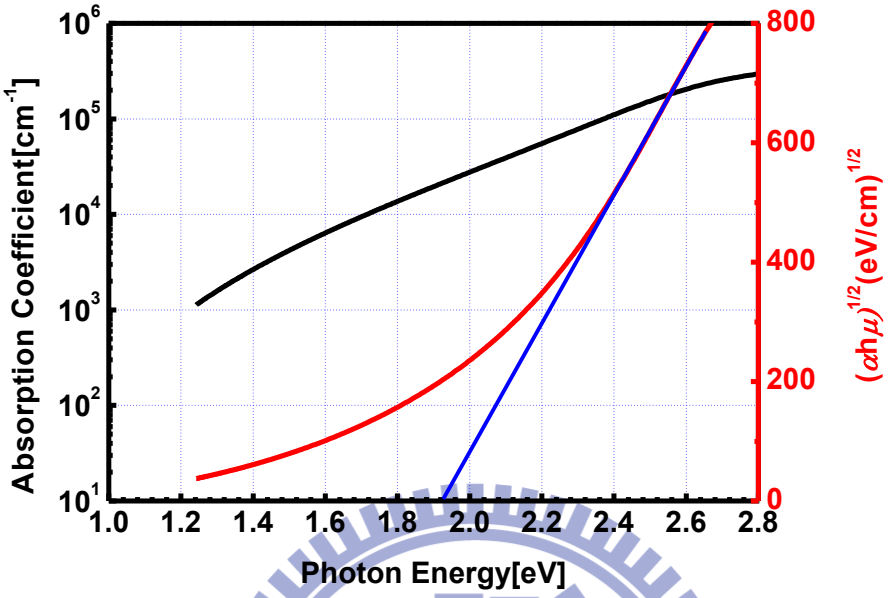

Figure 26 N-layer Absorption Coefficient Corresponds to the Photon Energy and Optical band gap fitting by Tauc Plot

layer	SiH_4	GeH_4	H_2	doping concentration	pressure	power	optical bandgap
p	10	200	200	10	900	60	1.9
i	15	150	150	-	700	30	1.89
n	10	200	200	5	900	60	1.91
SiGe	14	1	150	-	700	40	1.75
SiGe	13	2	200	-	700	40	1.62
SiGe	12	3	400	-	700	40	1.52
SiGe	10	2	200	-	700	40	1.61
SiGe	10	2	200	-	700	30	1.6
SiGe	10	2	200	-	700	20	1.52
SiGe	9	3	200	-	700	40	1.53
SiGe	9	3	400	-	700	40	1.52
SiGe	8	4	200	-	700	40	1.44
SiGe	8	4	400	-	700	40	1.49
SiGe	8	4	600	-	700	40	1.42
SiGe	6	6	600	-	700	40	1.35

Tabel 2 parameter and bandgap of amorphous silicon and amorphous silicon germanium

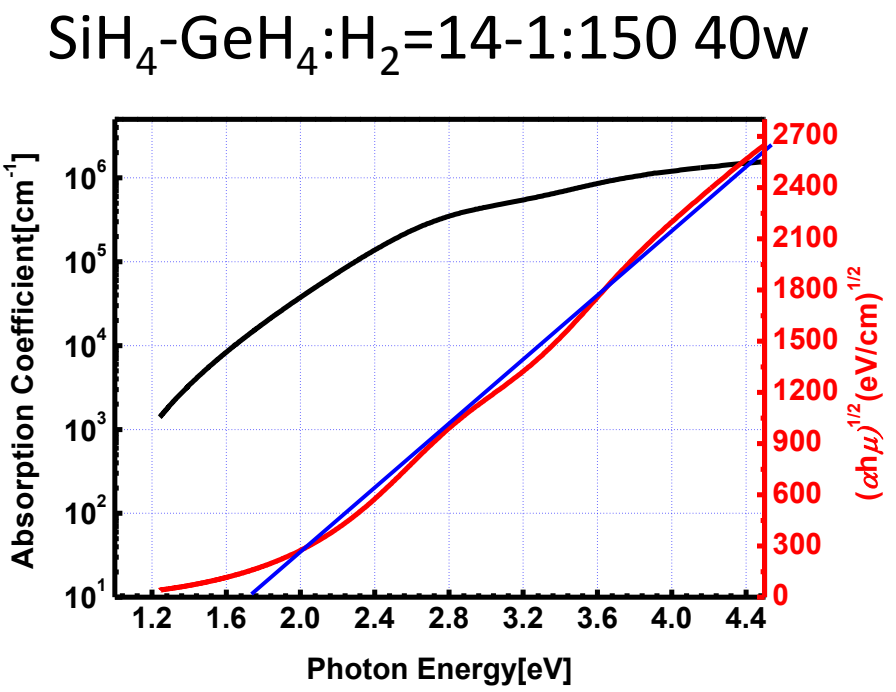

Figure 27 SiH_4-GeH_4:H_2=14-1:150 power=40w optical bandgap fitting

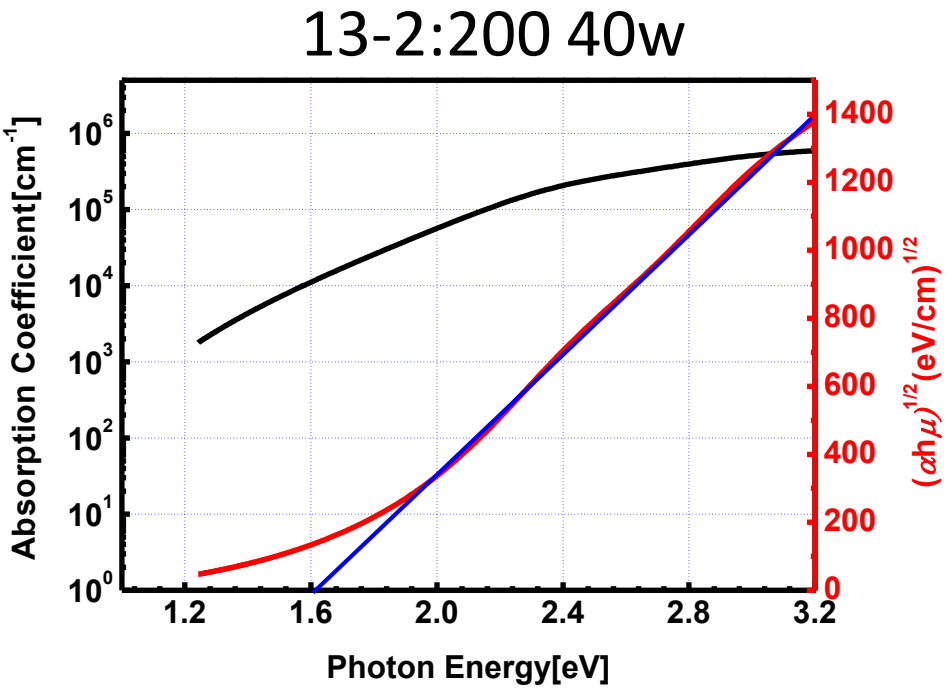

Figure 28 SiH_4-GeH_4:H_2=13-2:200 power=40w optical bandgap fitting

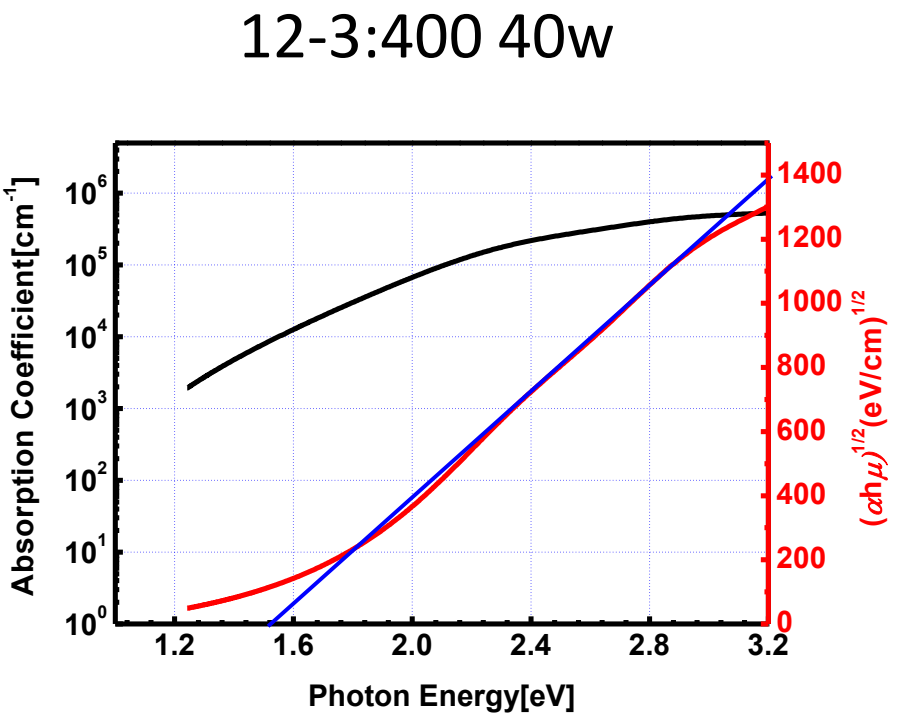

Figure 29 SiH_4-GeH_4:H_2=12-3:400 power=40w optical bandgap fitting

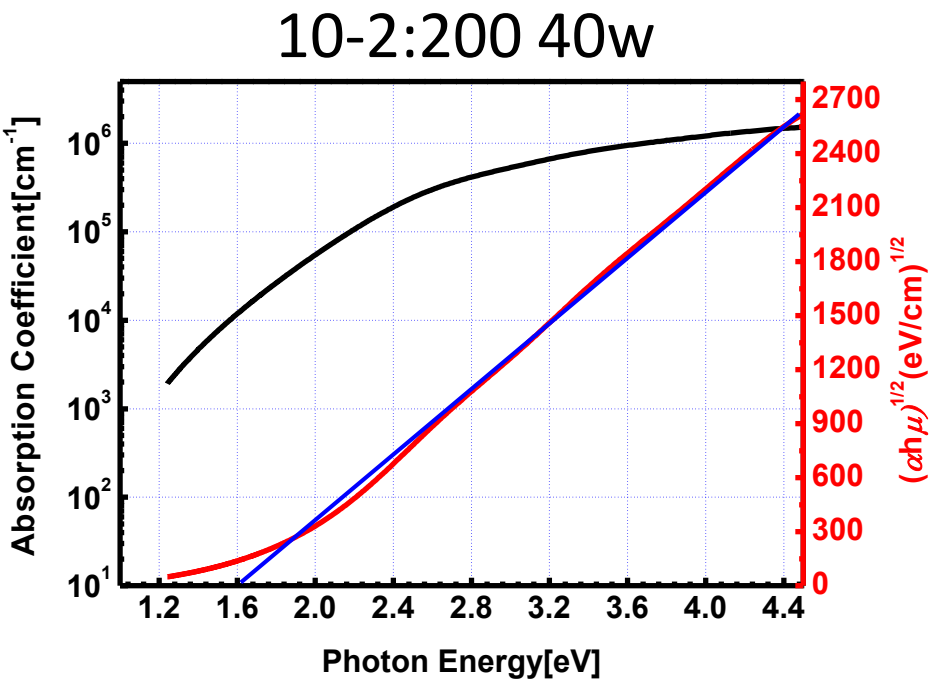

Figure 30 SiH_4-GeH_4:H_2=10-2:200 power=40w optical bandgap fitting

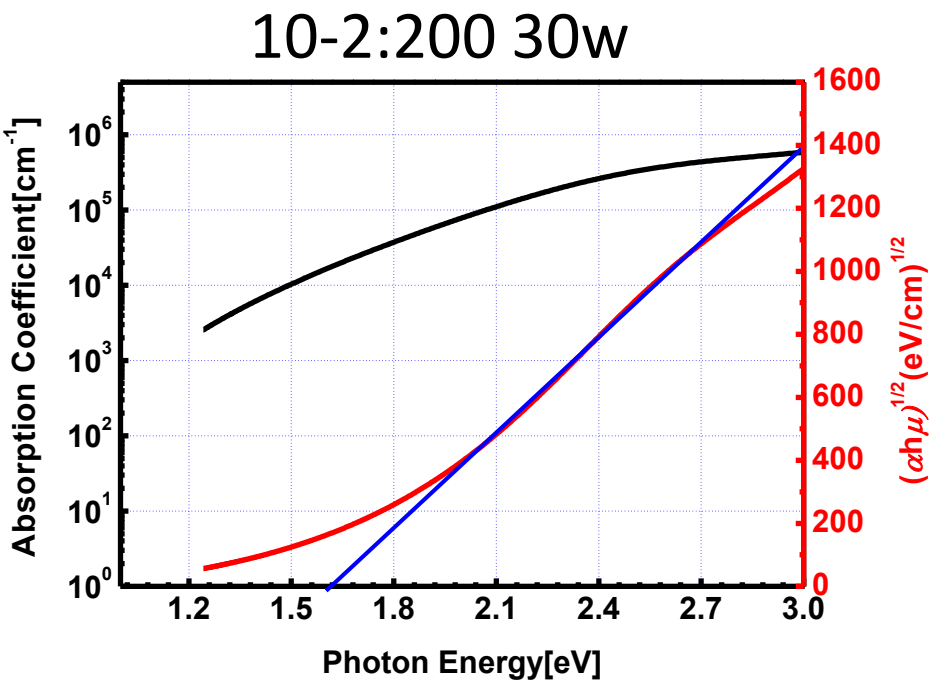

Figure 31 SiH_4-GeH_4:H_2=10-2:200 power=30w optical bandgap fitting

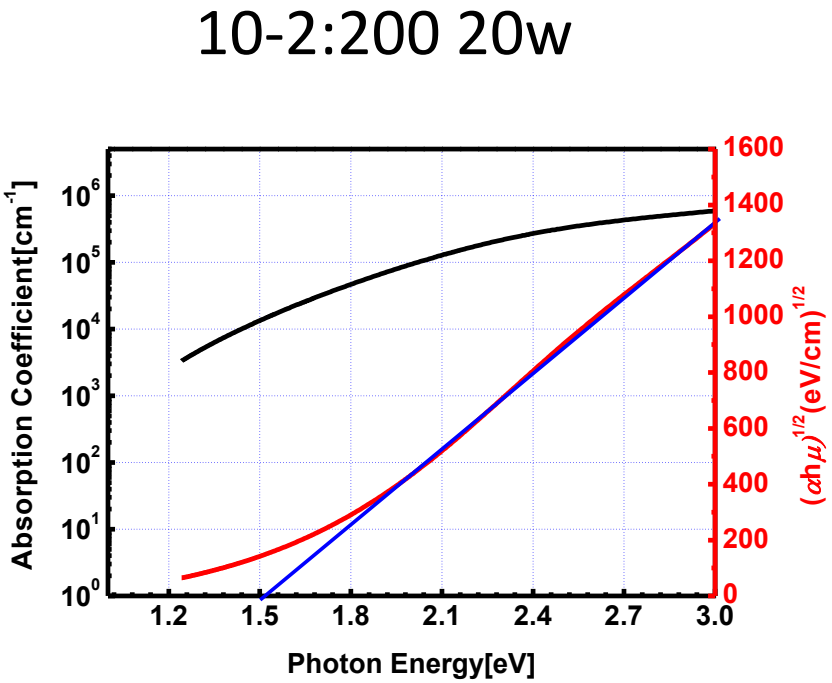

Figure 32 SiH_4-GeH_4:H_2=10-2:200 power=40w optical bandgap fitting

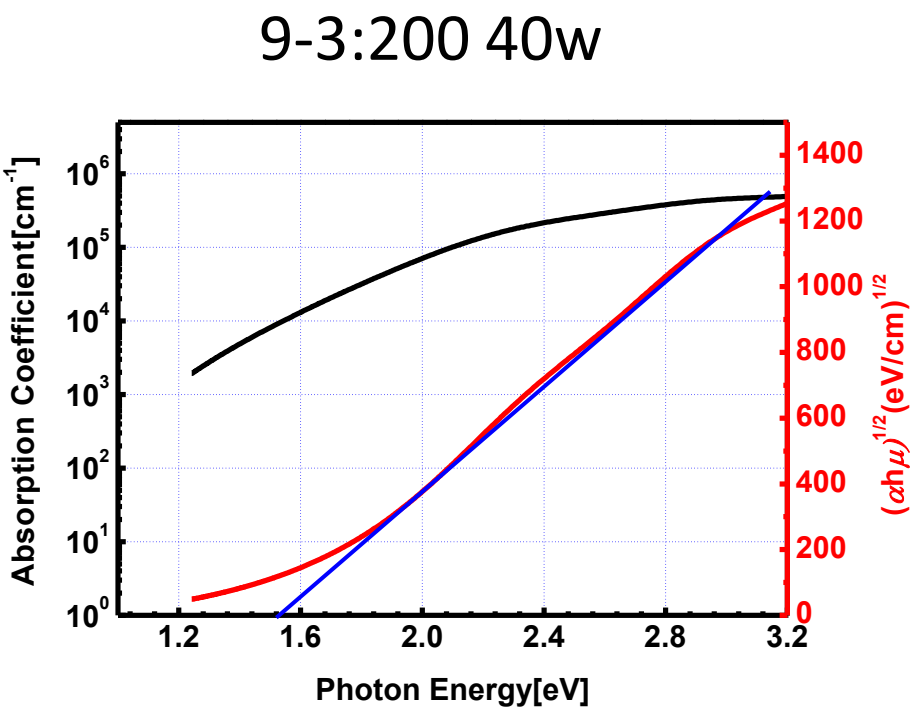

Figure 33 SiH_4-GeH_4:H_2=9-3:200 power=40w optical bandgap fitting

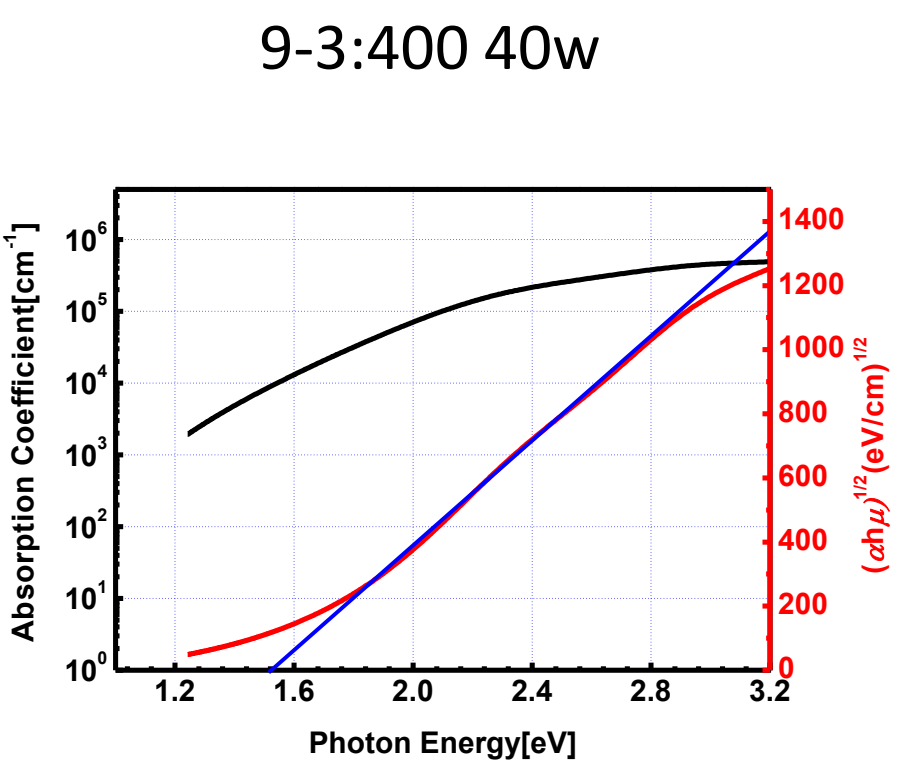

Figure 34 SiH_4-GeH_4:H_2=9-3:400 power=40w optical bandgap fitting

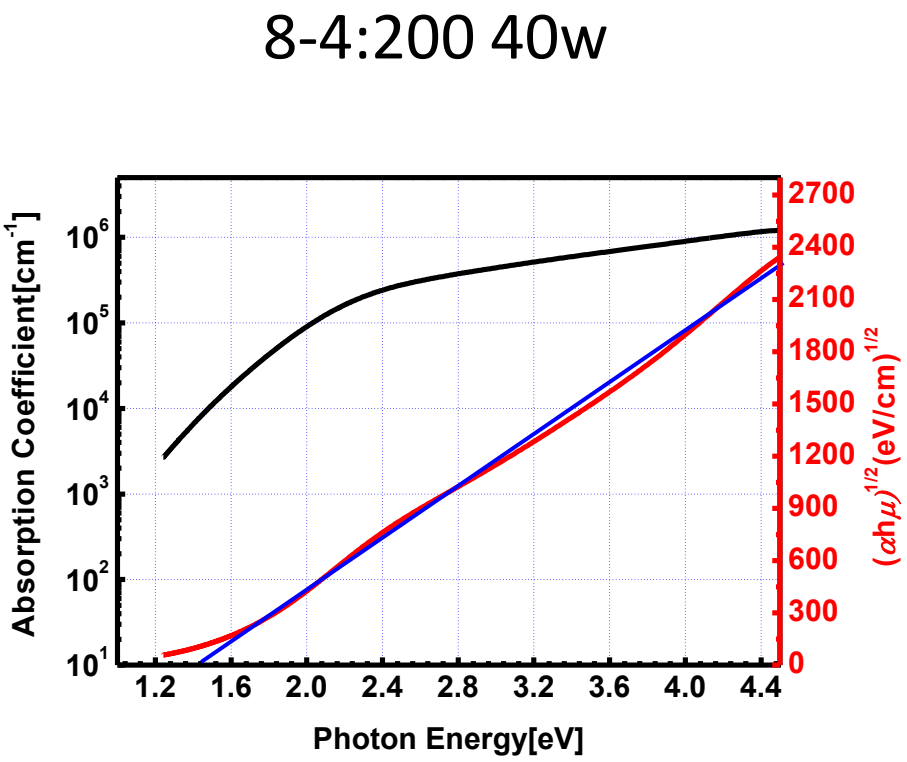

Figure 35 SiH_4-GeH_4:H_2=8-4:200 power=40w optical bandgap fitting

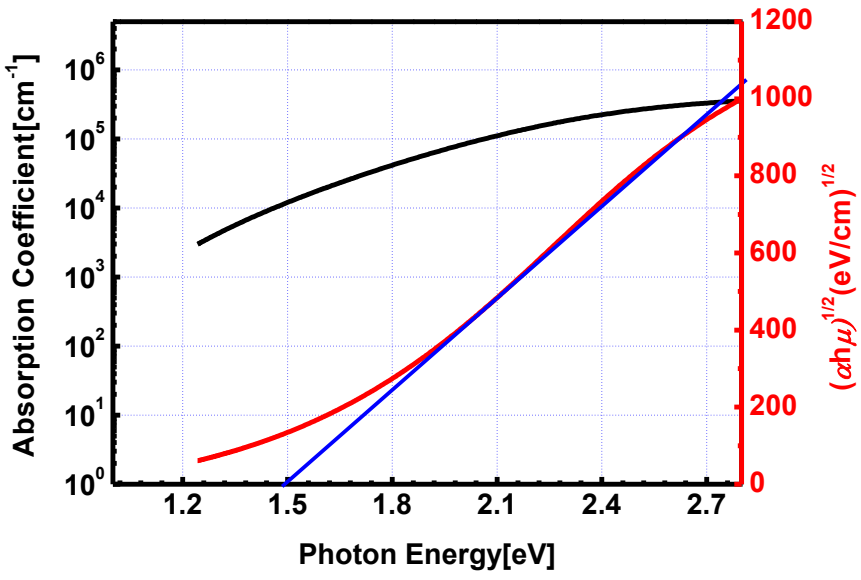

Figure 36 SiH_4-GeH_4:H_2=8-4:400 power=40w optical bandgap fitting

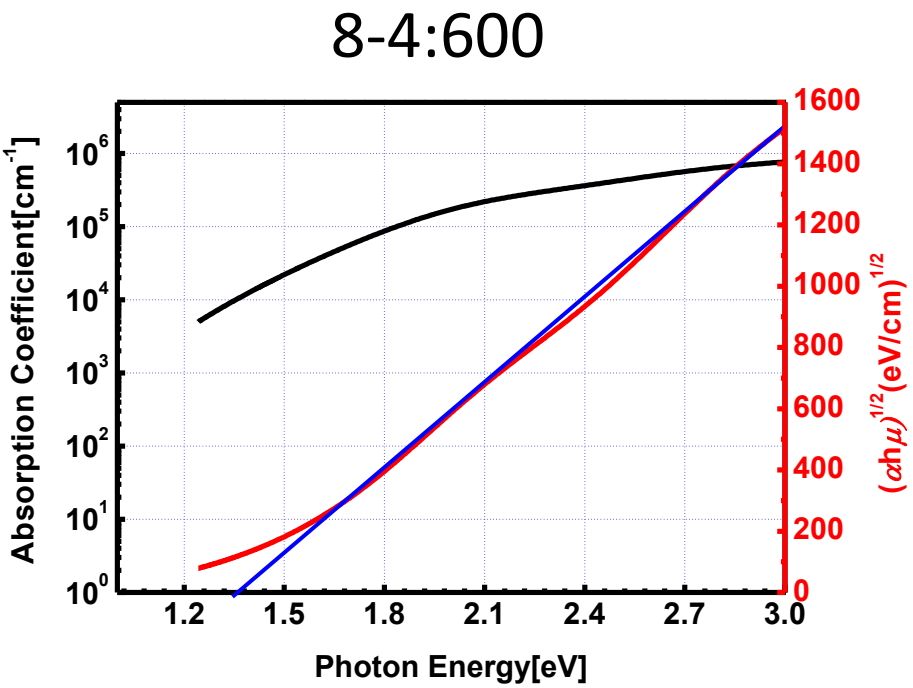

Figure 37 SiH_4-GeH_4:H_2=8-4:400 power=40w optical bandgap fitting

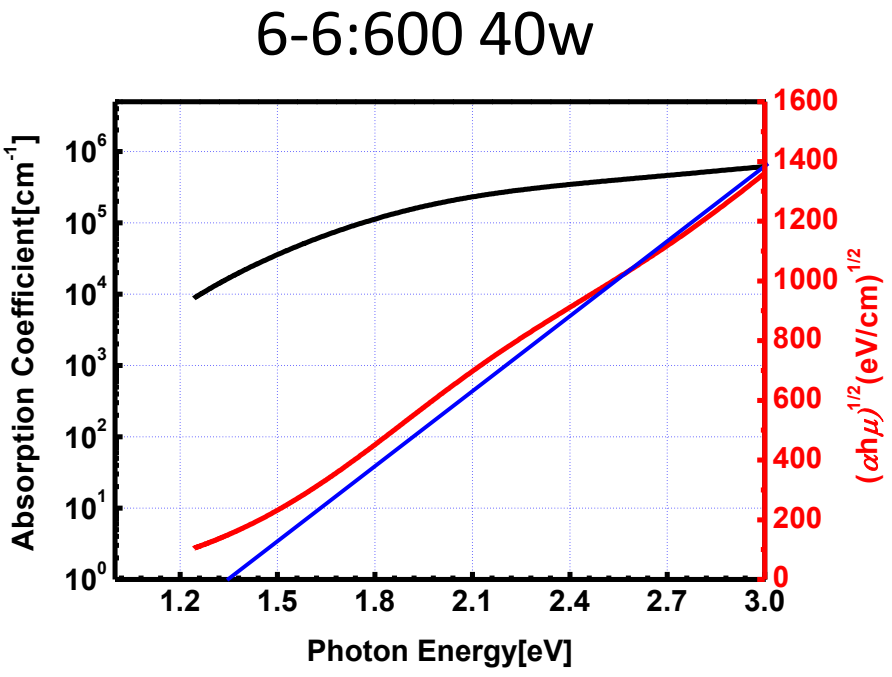

Figure 38 SiH_4-GeH_4:H_2=6-6:600 power=40w optical bandgap fitting

The **Figure 39** shows the reasonable growth rate is under 1.5A/s and the GeH_4/SiH_4+GeH_4 ration could be 0.06~0.18[6], which means the ratio we used was large enough to engineer the optical band gap.

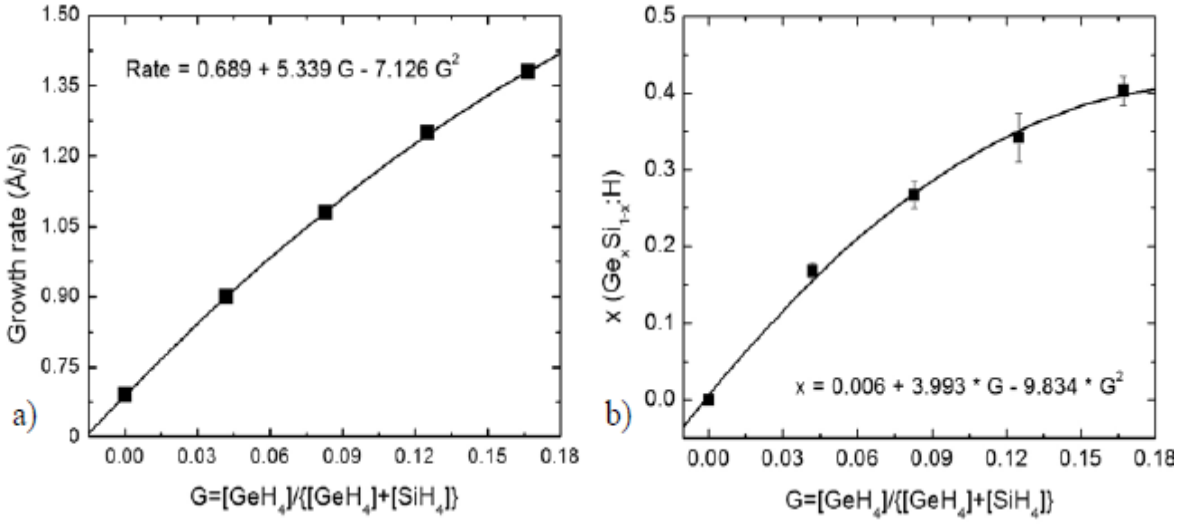

Figure 39 Growth Rate and GeH_4/SiH_4+GeH_4 Ratio

5.2 Amorphous Silicon and Silicon Germanium Alloy Single Junction Solar Cell

In last section, I have demonstrated the growth condition and optical band gap of each a-Si and a-SiGe layers. Now, I would show the result of a-Si:H, a-SiC;H and a-SiGe:H in various CH_4/SiH_4 and GeH_4/SiH_4 concentration with conversion efficiency and quantum efficiency.

5.2.1 Amorphous Silicon Thin Film Solar Cell

Figure 40 shows the structure of a-Si:H thin film solar cell. The glass substrate (Asahi(U)) is a commercial substrate which has deposited 900~1000 nm textured SnO_2:F. Then we deposited p-layer, i-layer, and n-layer step by step, after that we plated ITO and Al as back reflector and electrode. Our group has optimized the a-Si thin film solar cell. There are many size, including 3mm,5mm, and 10mm, in the one substrate. Each size has uniform performance, see **Figure 41**, and the conversion efficiency are more than 8%. Voc=0.88~0.9V, Jsc=15.5~16 mA/cm^2, FF achieves 57~62%, see **Figure 42**. The experimental result has almost fine tuned compared with the international quality.[2, 7-9]

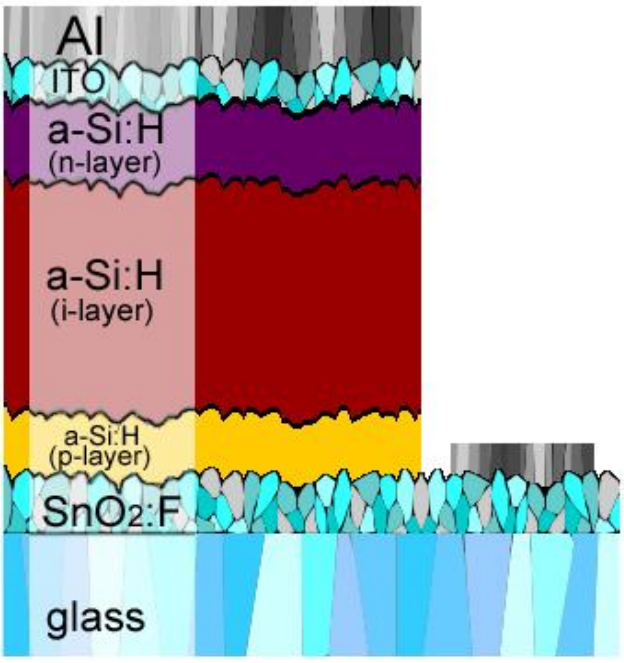

Figure 40 Structure of a-Si:H Thin Film Solar Cell

Width (mm)	V_{oc} (volt)	J_{sc} (mA/cm^2)	FF (%)	η (%)
3	0.88	16.0	57.5	8.08
5	0.89	15.9	62.0	8.78
10	0.89	15.4	62.6	8.57

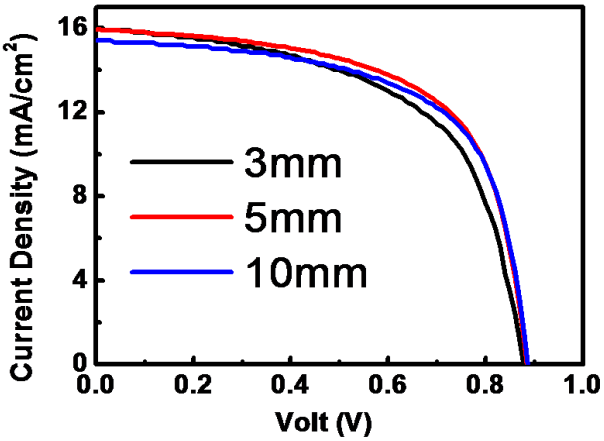

Figure 41 Voc, Jsc, FF and Conversion Efficiency of Each Size of Solar Cell

The TEM graph shows that the total thickness of p-i-n layer is about 400nm, and the thickness of ITO is about 80nm. The diffraction pattern clearly dedicates that the films in the device is amorphous structure.

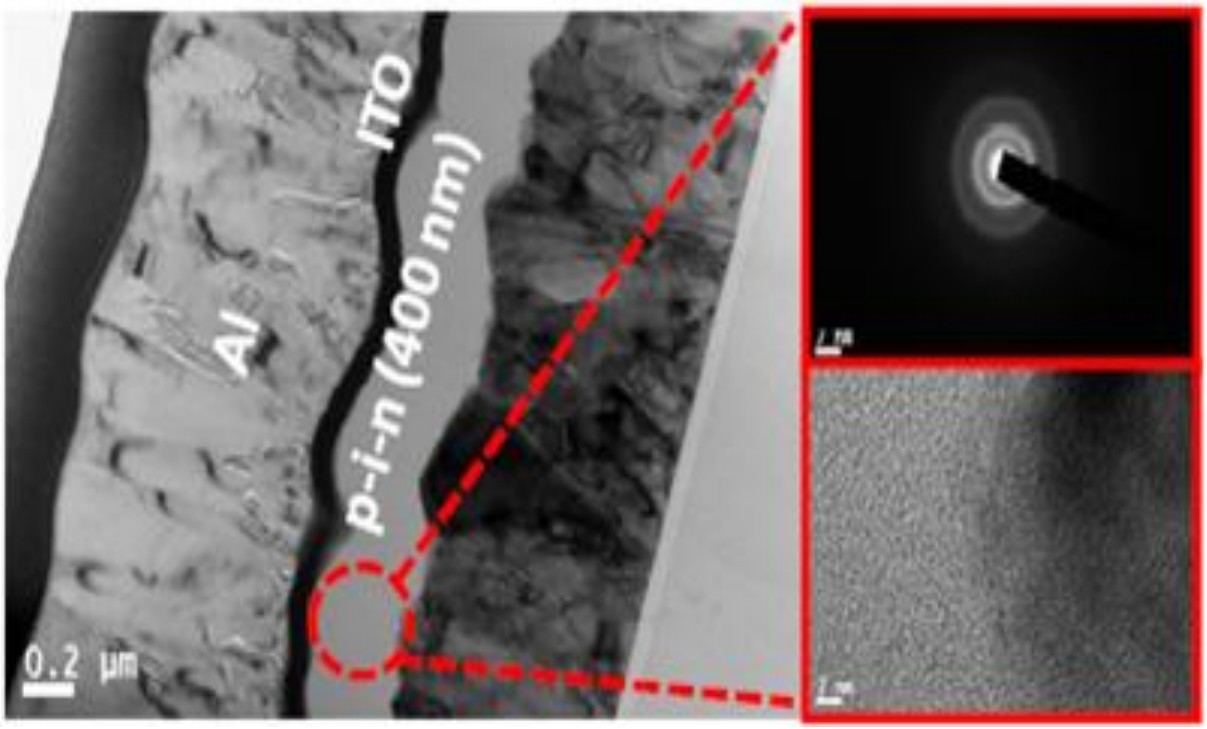

Figure 42 TEM Graph and Diffraction Pattern of a-Si Thin Film Solar Cell

5.2.2 Amorphous Silicon Germanium Thin Film Solar Cell

I have briefly discussed the structure and performance of a-Si thin film solar cell fabricated by our group in section **5.1.1** and **5.2.2**. Now I would demonstrate the amorphous silicon germanium thin film solar cells by various GeH_4/SiH_4 concentrations a-SiGe thin film. My research foundation established in the high efficiency and high uniformity a-Si thin film solar cell, so I used the similar structure, see **Figure 43**, and parameter with GeH_4 gas inflow at the beginning. I fixed the pressure at 700mtorr, i-layer thickness 300nm and RF power = 40w to vary the GeH_4/SiH_4+GeH_4 ratio, the result shows in **Table 3**. The data clearly shows that the conversion efficiency dramatically decreased as GeH_4/SiH_4+GeH_4 ratio increased. The reason might be that as the ratio becomes larger, the absorption increased dramatically and defect become much more, so maybe I should try the thinner a-SiGe i-layer when I used the higher GeH_4/SiH_4+GeH_4 ratio. Fortunately, the QE response obviously increased in 700~800nm, Which means that the lower optical band gap truly plays the role.

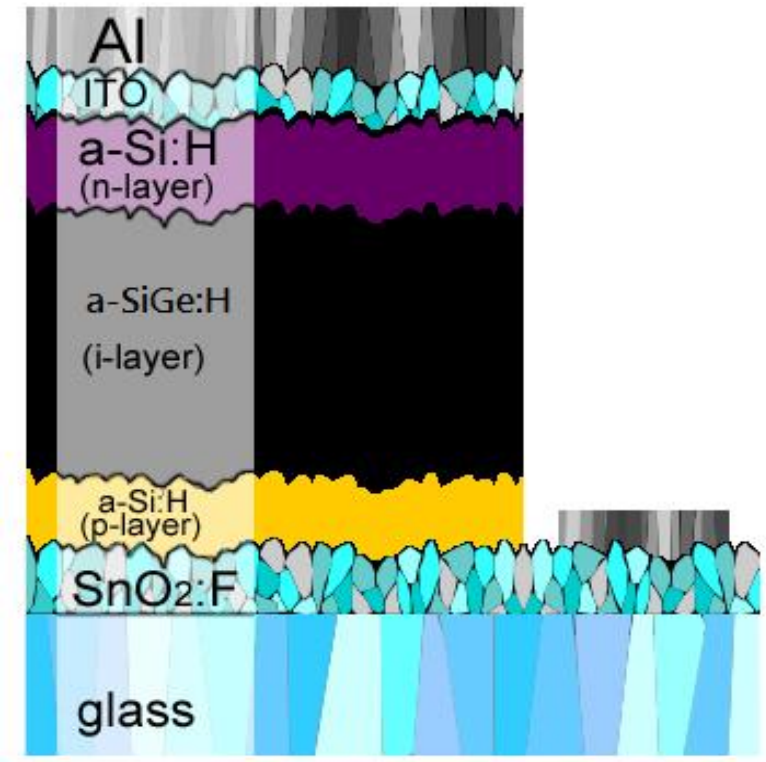

Figure 43 The Structure of a-SiGe:H Thin Film Solar Cell

SiH_4-GeH_4 :H_2	i-layer Thickness	pressure	power	V_{oc}	J_{sc}	FF	η
sccm	nm	mtorr	40	(volt)	(mA/cm^2)	(%)	(%)
14-1:150	300	700	40	0.83	17.07	50.5	7.16
10-2:200	300	700	40	0.74	13.1	43.8	4.25
8-4:200	300	700	40	0.44	8.31	27.8	1.01

Table 3 The result of a-SiGe thin film solar cell by varying GeH_4/SiH_4+GeH_4 ratio

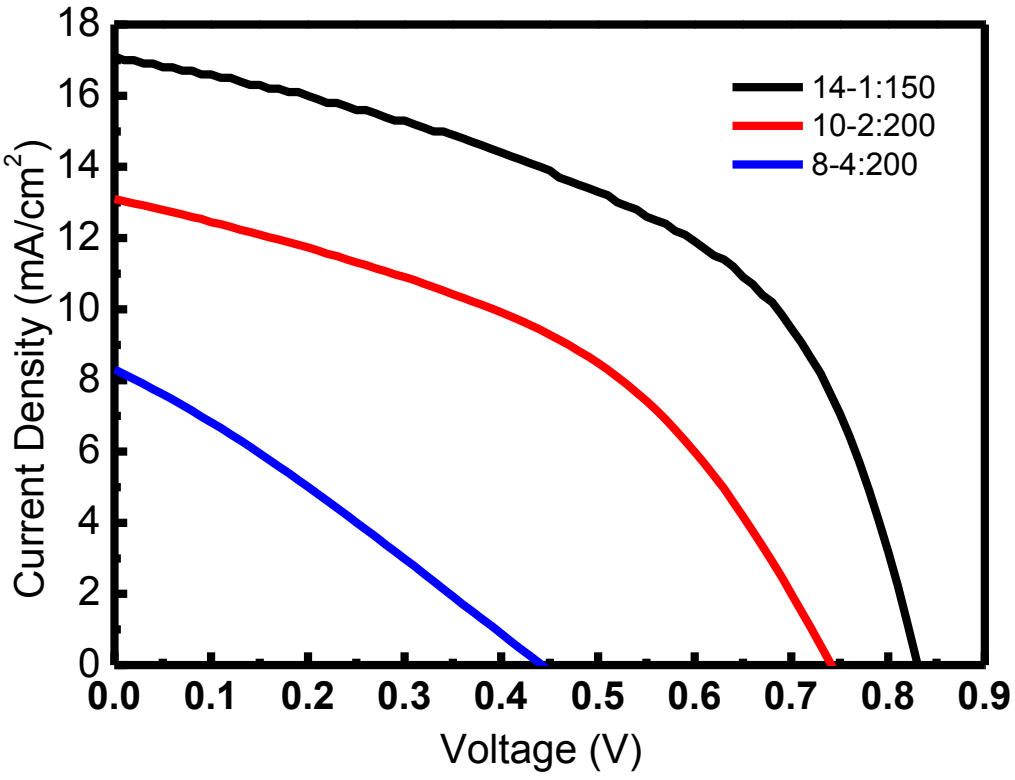

Figure 44 I-V Curve of a-SiGe Thin Film Solar Cell by Varying GeH_4/SiH_4+GeH_4 Ratio

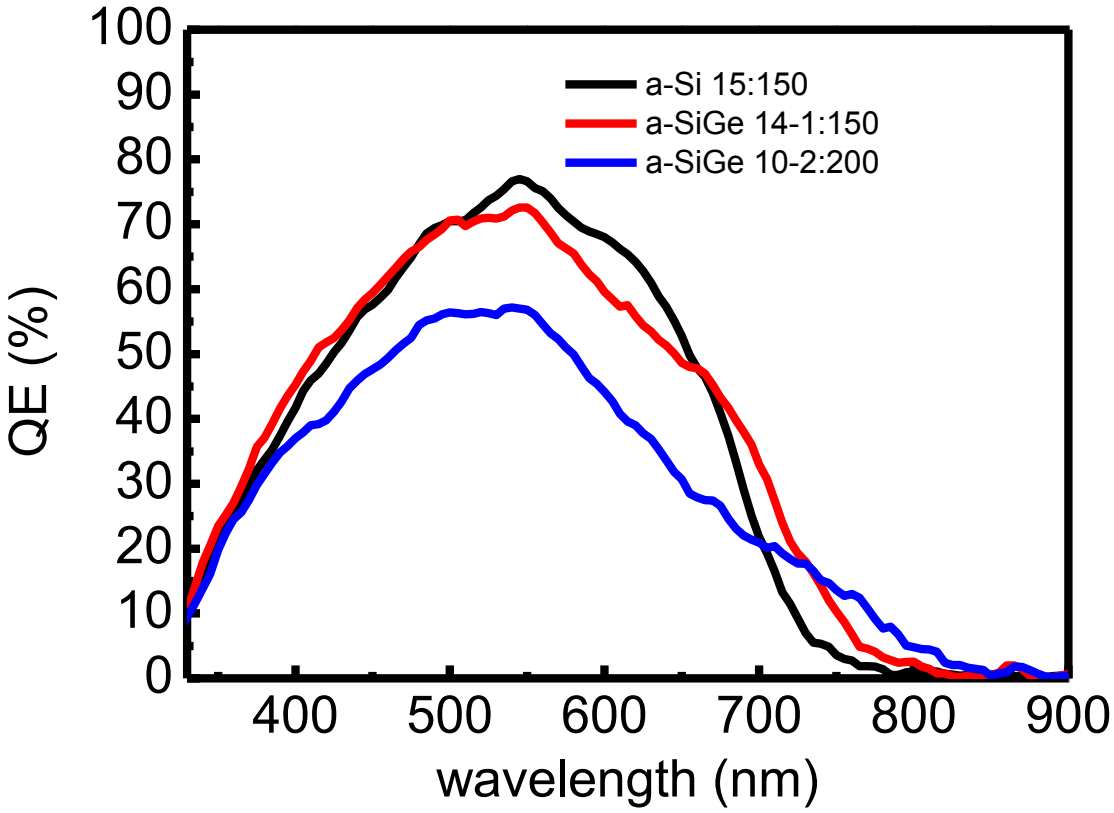

Figure 45 The QE of a-SiGe thin film solar cell by varying GeH_4/SiH_4+GeH_4 ratio

After that, I decreased the a-SiGe i-layer thickness to 200nm and try to vary the H_2 inflow, the result shows in **Table 4** and **Figure 46 47**. Although the conversion efficiency became poor, we can still find out that the open circuit voltage had decreased to less than 0.65V and the QE respond extended to 900nm.

SiH_4-GeH_4: H_2	i-layer Thickness	pressure	power	V_{oc}	J_{sc}	FF	η
sccm	nm	mtorr	40	(volt)	(mA/cm^2)	(%)	(%)
9-3:200	200	700	40	0.62	11.56	50.4	3.61
9-3:400	200	700	40	0.5	10.6	41.6	2.31
8-4:400	200	700	40	0.59	12.49	49.1	3.62
8-4:600	200	700	40	0.31	7.04	30.3	0.66
8-4:800	200	700	40	0.22	6.15	22.9	0.36

Table 4 The result of a-SiGe thin film solar cell by varying H_2 inflow

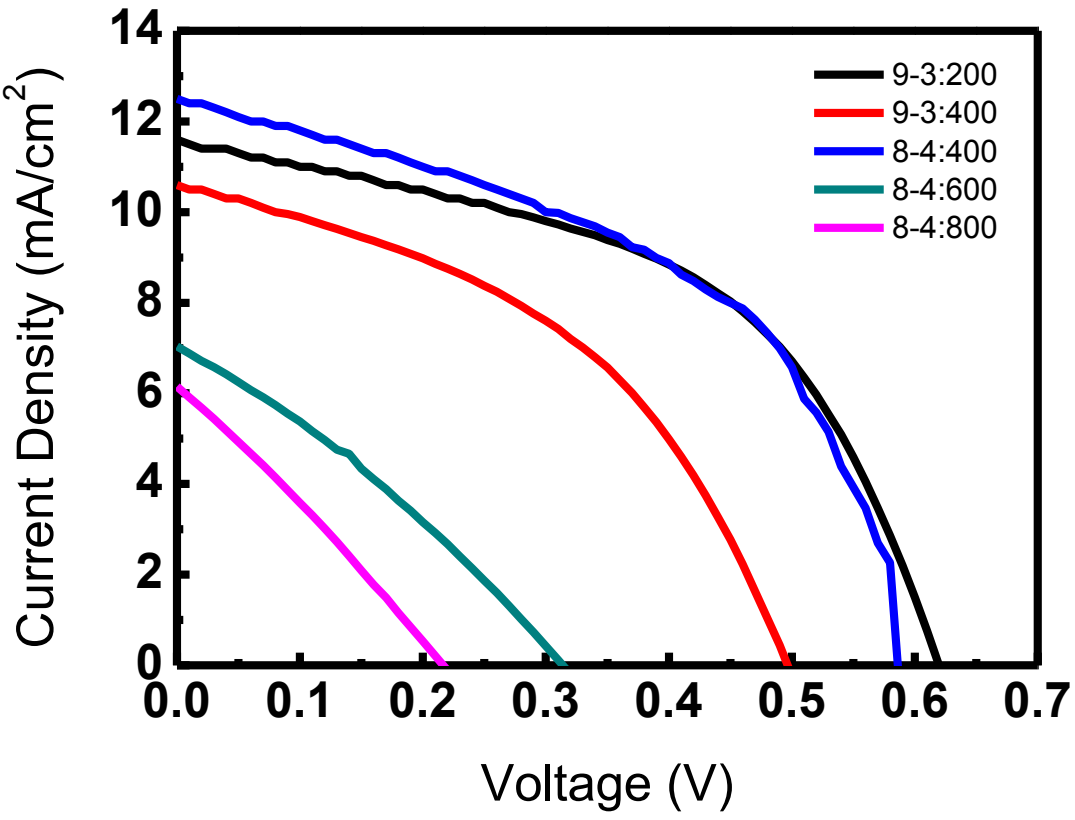

Figure 46 I-V Curve of a-SiGe Thin Film Solar Cell by Varying H_2 Inflow

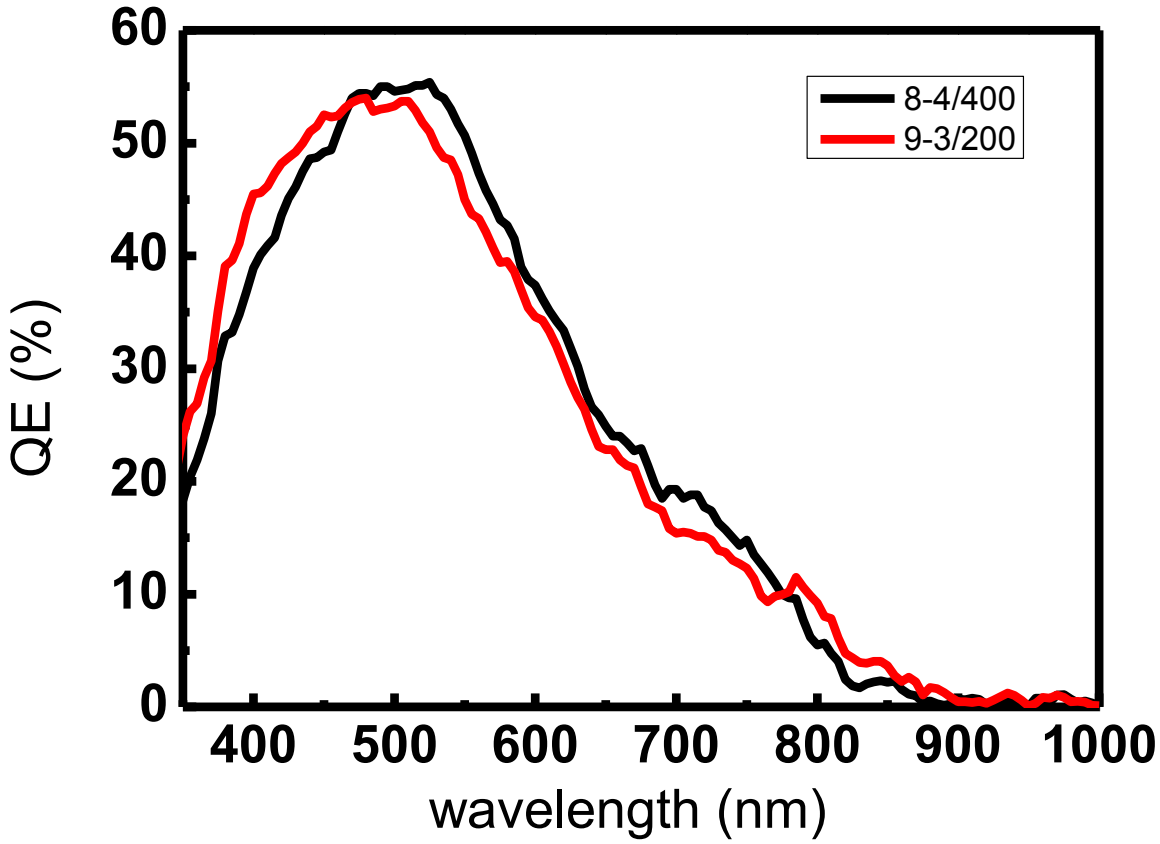

Figure 47 QE Response of a-SiGe Thin Film Solar Cell by Varying H_2 Inflow

Furthermore, I have also varied the pressure, 700~1000 mtorr of a-SiGe:H deposited with different GeH_4/SiH_4+GeH_4 ratio. As the GeH_4/SiH_4+GeH_4 ratio is higher (SiH_4-GeH_4:H_2=10-2:250), the process pressure should be higher. And when the GeH_4/SiH_4+GeH_4 ratio is lower (SiH_4-GeH_4:H_2=14-1:150), then the process pressure should be lower.

SiH_4-GeH_4:H_2	i-layer Thickness	pressure	power	V_{oc}	J_{sc}	FF	η
sccm	nm	mtorr	40	(volt)	(mA/cm^2)	(%)	(%)
10-2:250	150	700	35	0.48	12.13	32.5	1.891
10-2:250	150	900	35	0.58	12	32	2.229
10-2:250	150	700	40	0.61	12.27	34.2	2.564
10-2:250	150	900	40	0.62	13.51	40.1	3.355
14-1:150	150	900	40	0.8	14.3	47.2	5.41
14-1:150	150	1000	40	0.79	14.05	45.7	5.07
14-1:150	200	900	40	0.77	13.95	48.3	5.18

Table 5. The result of a-SiGe thin film solar cell by varying GeH_4/SiH_4+GeH_4 ratio and pressure

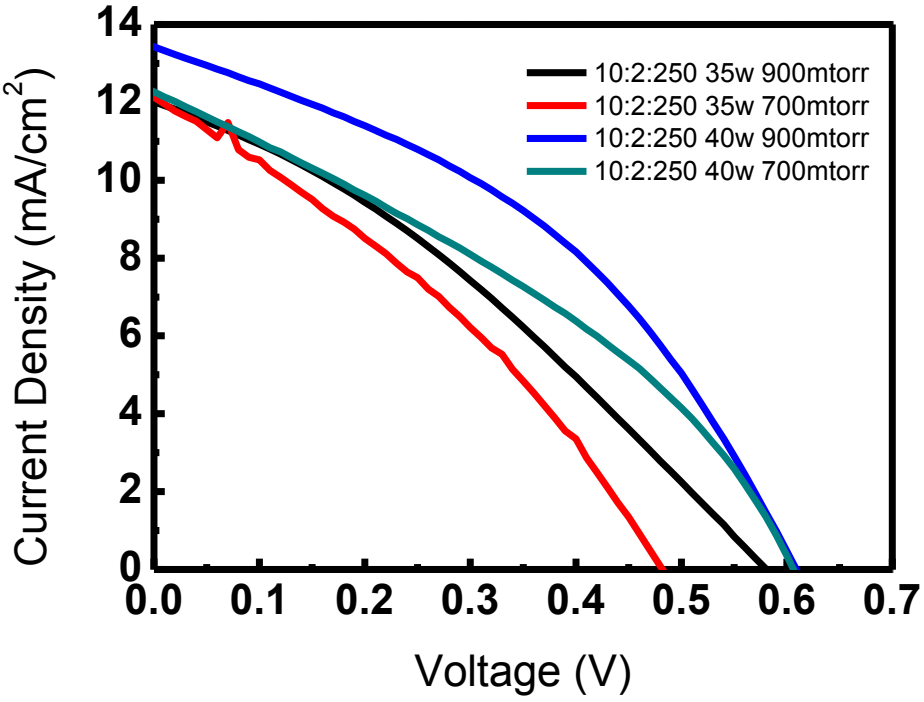

Figure 48 I-V Curve of a-SiGe Thin Film Solar Cell by Varying pressure and power

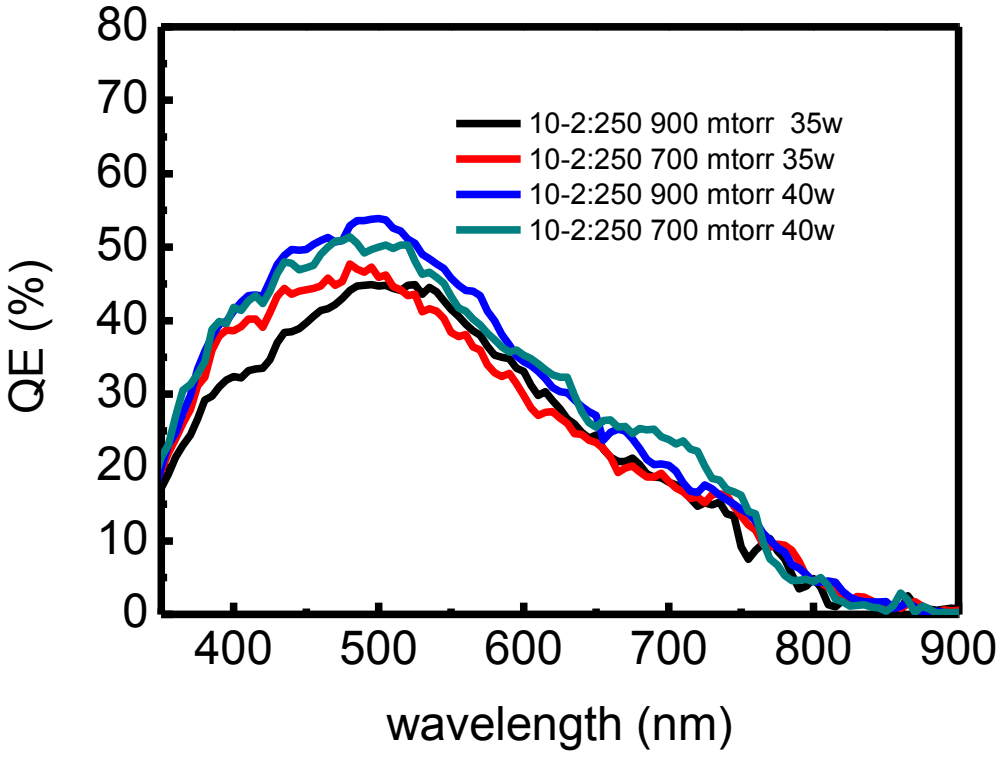

Figure 49 QE responds of a-SiGe Thin Film Solar Cell by Varying pressure and power

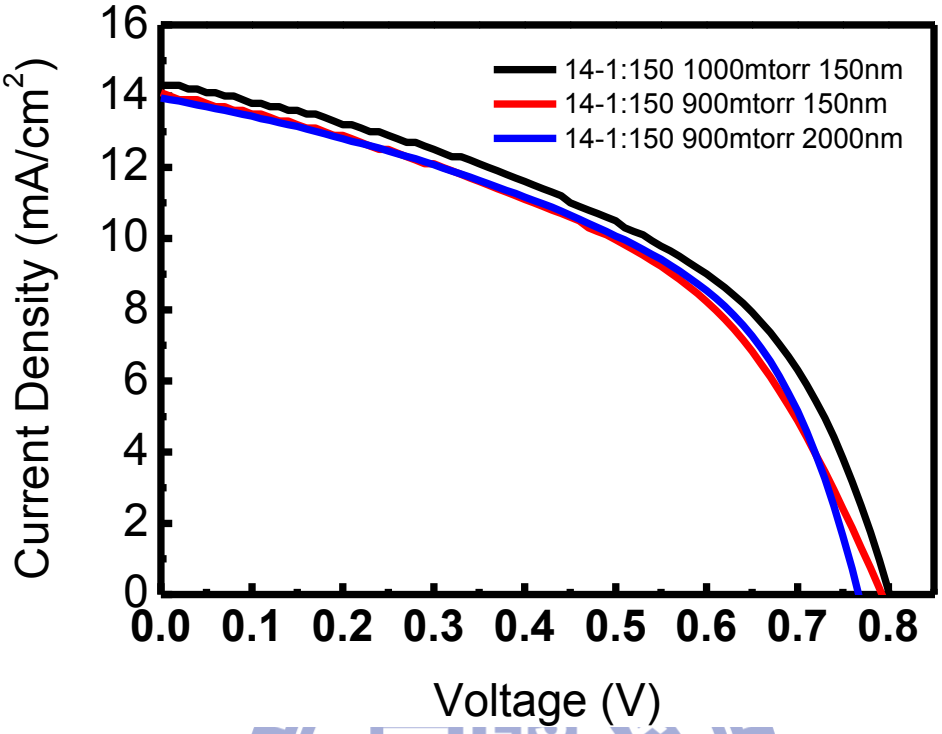

Figure 50 I-V Curve of a-SiGe Thin Film Solar Cell by Varying thickness and pressure

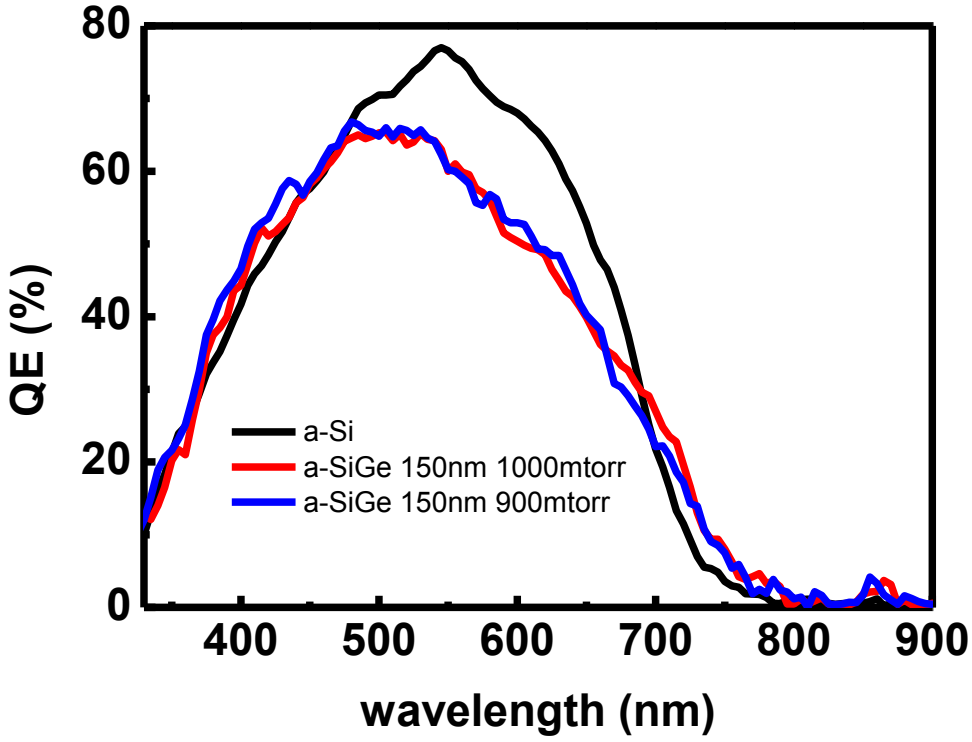

Figure 51 QE Responds of a-SiGe Thin Film Solar Cell by Varying pressure and Thicknesss


E S A
1896

5.2.3 Amorphous Silicon Carbide Thin Film Solar Cell

In this section, I would demonstrate the amorphous silicon carbide thin film solar cell. Because of the optical band gap of a-SiC (1.9~2eV) is higher than a-Si, its main function is to increase the absorption of the range of solar spectra from 300~500nm. As we knew, the short wave length in visible light would be absorb in shallow part of thin film solar cell, therefore, I just used a-SiC:H in p-layer, see **Figure 52**, and I used the same i-layer and n-layer in the a-Si thin film solar cell. The result shows that we just only used the a-SiC with 8~10nm and the absorption in short wavelength (300~550nm) increased obviously. Even though the conversion efficiency would not improve, but we can still used the feature in the tandem solar cell.

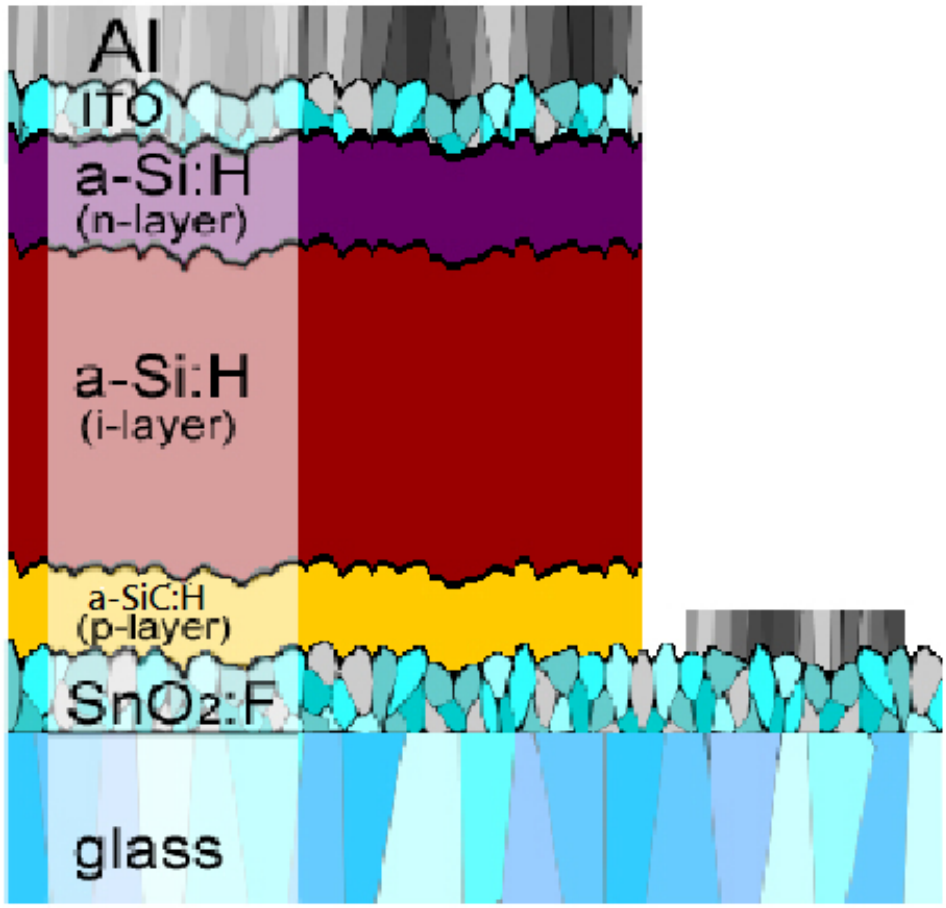

Figure 52 Structure of a-SiC:H Thin Film Solar Cell

SiH_4-CH_4:H_2	p-layer a-SiC + a-Si thickness	pressure	power	V_{oc}	J_{sc}	FF	η
sccm	nm	mtorr	40	(volt)	(mA/cm^2)	(%)	(%)
8-2:200	12 + 0	900	60	0.8	15.48	50.9	6.38
8-2:200	10 + 2	900	60	0.83	15.31	56.2	7.14
8-2:200	8 + 4	900	60	0.86	14.95	62.2	7.99

Table 6 Result of a-SiC:H Thin Film Solar Cell

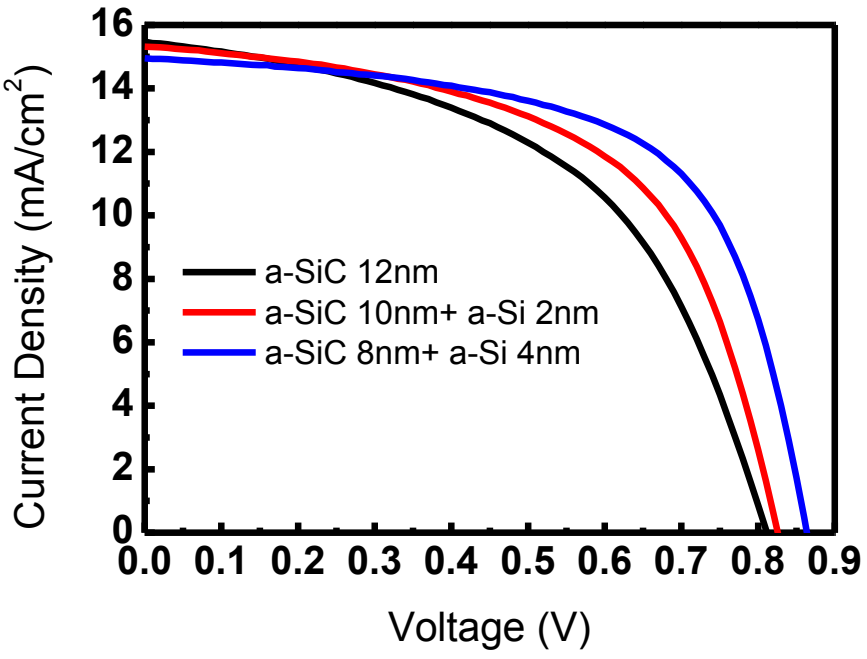

Figure 53 I-V Curve of a-SiC:H Thin Film Solar Cell

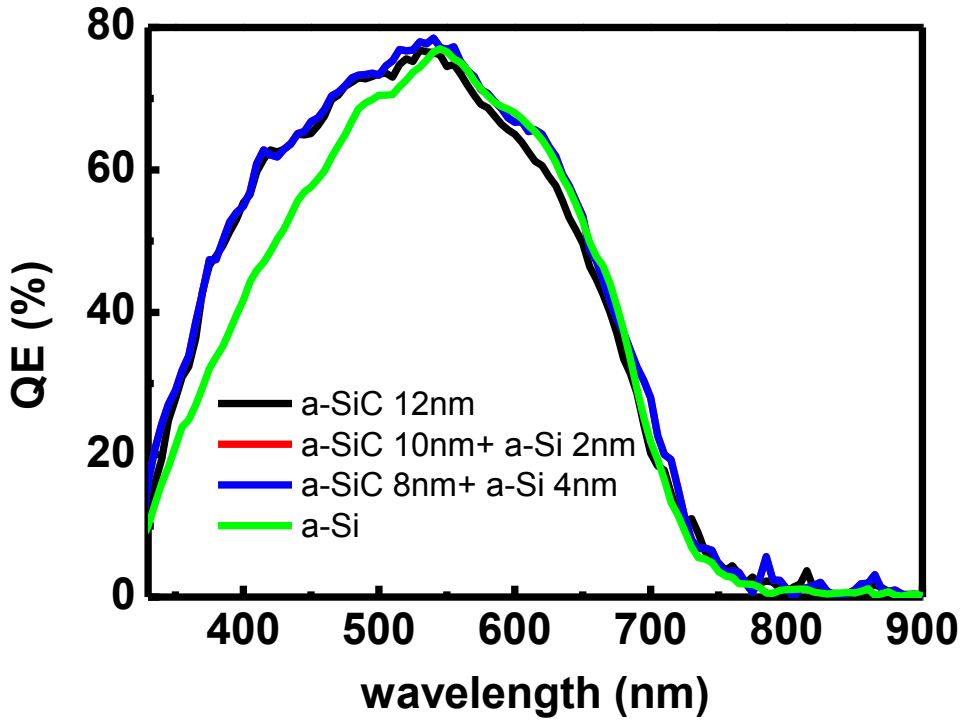

Figure 54 QE Responds of a-SiC:H Thin Film Solar Cell

5.3 Double Junction and Triple Junction Solar Cell

In this section, I will demonstrate double junction tandem solar cell and triple junction solar cell. The main purpose to fabricate muti-junction solar cell was that we wanted to utilize the full solar spectra efficiently. So, I would combined the a-Si and a-SiGe thin film solar cell to a double junction and triple junction thin film soalr cell.

5.3.1 a-Si/a-Si Tandem Solar Cell

Although a-Si/a-Si tandem solar cell (the structure is like **Figure 55**) doesn't have different optical band gap as others, we can also utilize it to learn how to fabricate a double junction solar cell. In our experiment result, we found that there are two important concept. First, we should use thinner i-layer in top cell and thicker i-layer in bottom cell. Second, the doping concentration of n-layer in top cell is quite important. In our experimental result, see **Figure 56~57,** if we used lower doping concentration in n-layer of top cell, the opev circuit voltage could achieve 1.6V, then we can get better conversion efficiency.

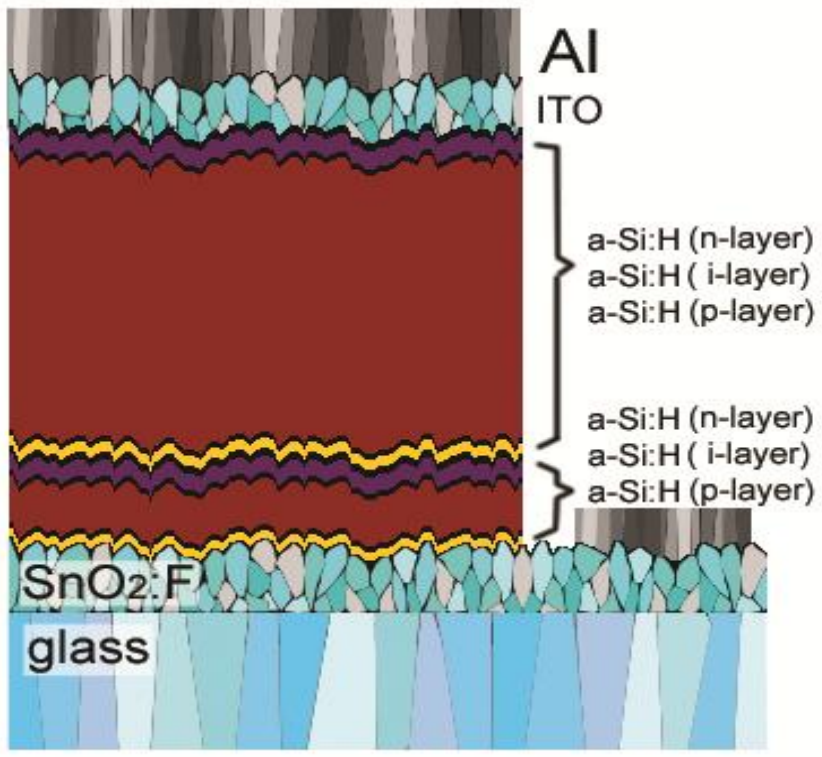

Figure 55 Structure of a-Si/a-Si Tandem Solar Cell

	i-layer Thickness	n-layer dopant concentration	V_{oc}	J_{sc}	FF	η
	nm	%	(volt)	(mA/cm^2)	(%)	(%)
top cell	75	1.33	0.92	8.4	61.9	4.79
bottom cell	350	5				
top cell	100	5	1.6	6.4	63.9	6.54
bottom cell	250	5				

Table 7 Result of a-Si/a-Si Tandem Solar Cell

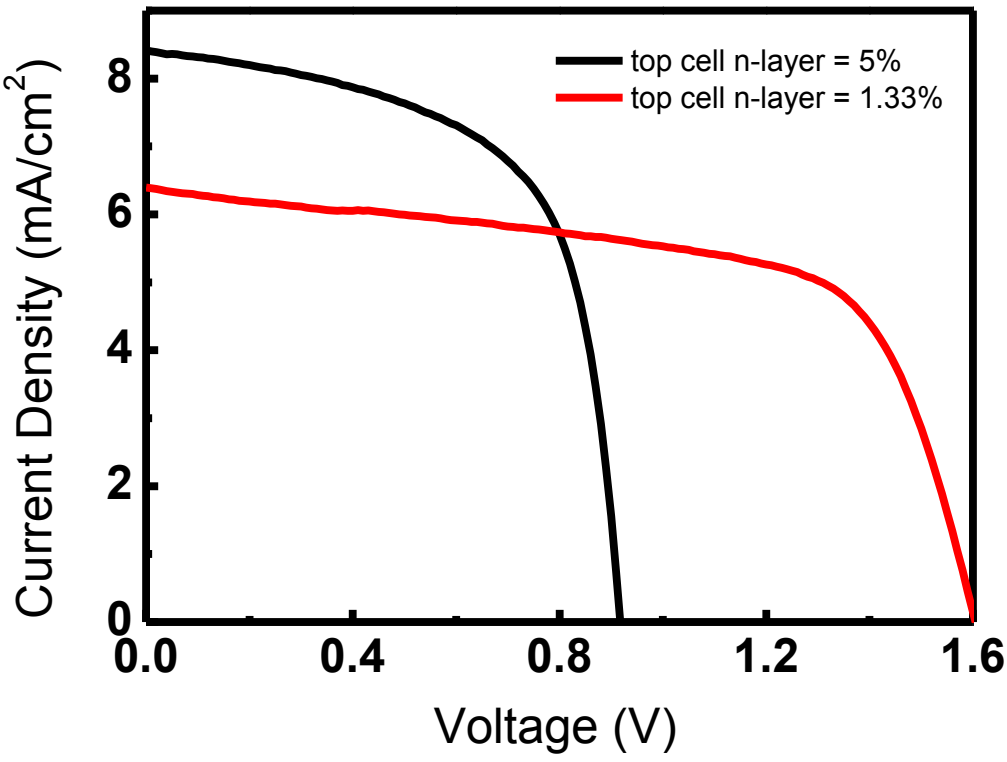

Figure 56 I-V curve of a-Si/a-Si Tandem Solar Cell

5.3.2 a-Si/a-SiGe Tandem Solar Cell

In the result of last section, I have found thickness of i-layer in each two junction and doping concentration of n-layer in top junction were both really important. First, I used two different GeH_4/SiH_4+GeH_4 Ratio a-SiGe i-layer on bottom cell, and the doping concentration of n-layer on top cell is 5%. We found the FF was bad and the open circuit voltage was low, see **Table 8** and **Figure 57**. That means we should used lower GeH_4/SiH_4+GeH_4 Ratio a-SiGe i-layer on bottom cell amd doping concentration of n-layer on top cell.

	SiH_4-GeH_4:H_2	**i-layer thickness**	**n-layer dopant concentration**	**V_{oc}**	**J_{sc}**	**FF**	**η**
	sccm	nm	%	(volt)	(mA/cm^2)	(%)	(%)
top cell	15:150	100	5	0.95	6.93	42.3	2.78
buttom cell	8-4:400	150	5				
top cell	15:150	100	5	1.1	5.54	49.5	3.01
buttom cell	9-3:300	150	5				

Table 8 Result of a-Si/a-SiGe Tandem Solar Cell Varying the GeH_4/SiH_4+GeH_4 Ratio on Bottom Cell

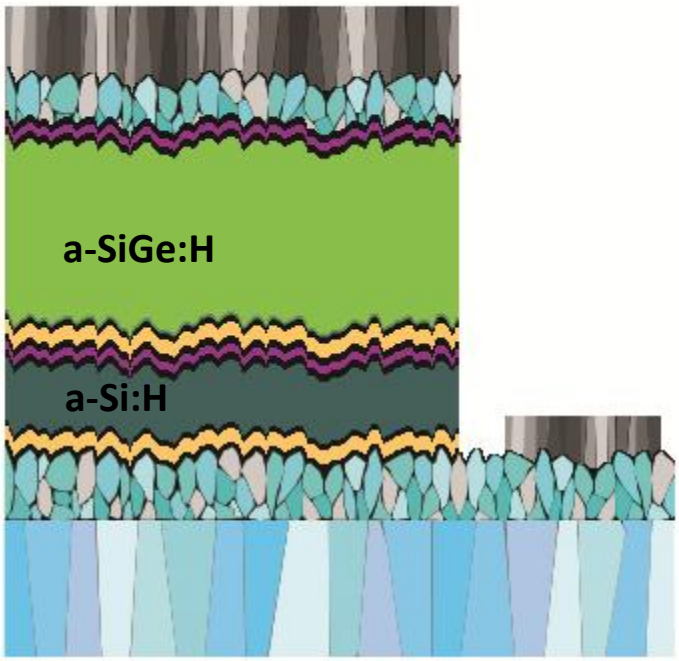

Figure 57 Structure of a-Si/a-SiGe Tandem Solar Cell

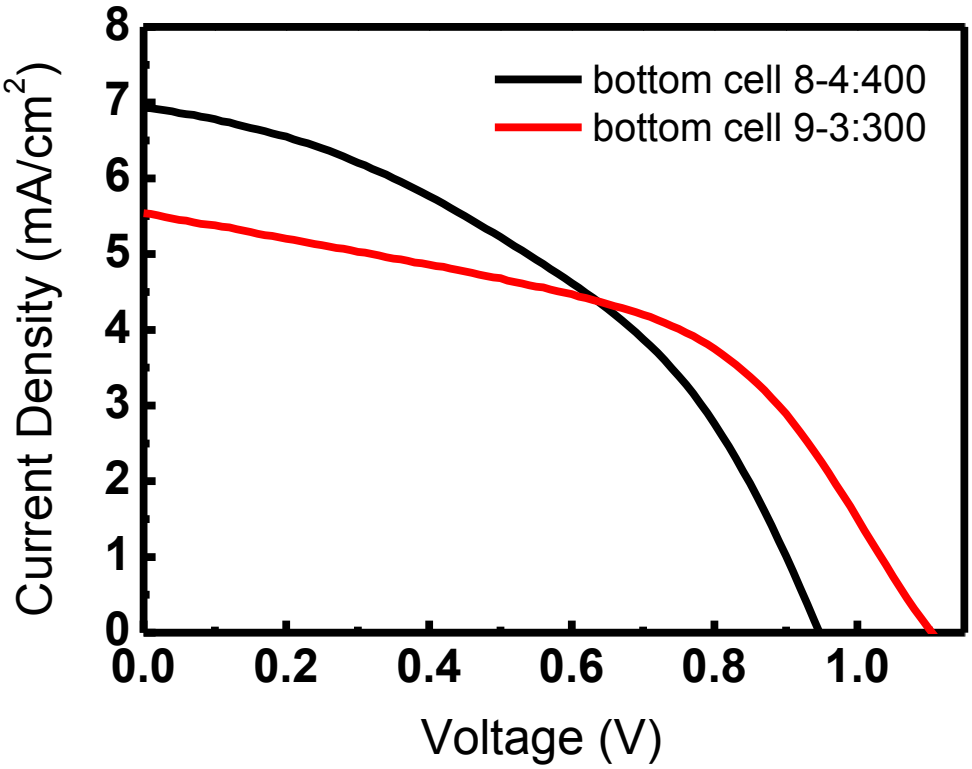

Figure 58 I-V Curve of a-Si/a-SiGe Tandem Solar Cell Varying the GeH_4/SiH_4+GeH_4 Ratio on Bottom Cell

After that, I changed the GeH_4/SiH_4+GeH_4 Ratio to 10-2:150 and the doping concentration of n-layer on top cell to 1.5%, then fixed it. This time I varied the i-layer thickness of top cell. The result shows that the Voc increased to more than 1.3V and the Jsc was larger when i-layer thickness of top cell was up to 100nm, see **Table 8** and **Figure 59**.

	SiH_4-GeH_4 :H_2	**i-layer Thickness**	**n-layer dopant concentration**	**V_{oc}**	**J_{sc}**	**FF**	**η**
	sccm	nm	%	(volt)	(mA/cm^2)	(%)	(%)
top cell	15:150	100	1.5	1.36	7.59	43.9	4.53
buttom cell	10-2:250	150	5				
top cell	15:150	75	1.5	1.35	7.06	46.6	4.48
buttom cell	10-2:250	150	5				
top cell	15:150	50	1.5	1.33	6.35	58.3	4.91
buttom cell	10-2:250	150	5				

Table 8 Result of a-Si/a-SiGe Tandem Solar Cell Varying the GeH_4/SiH_4+GeH_4 Ratio on Bottom Cell

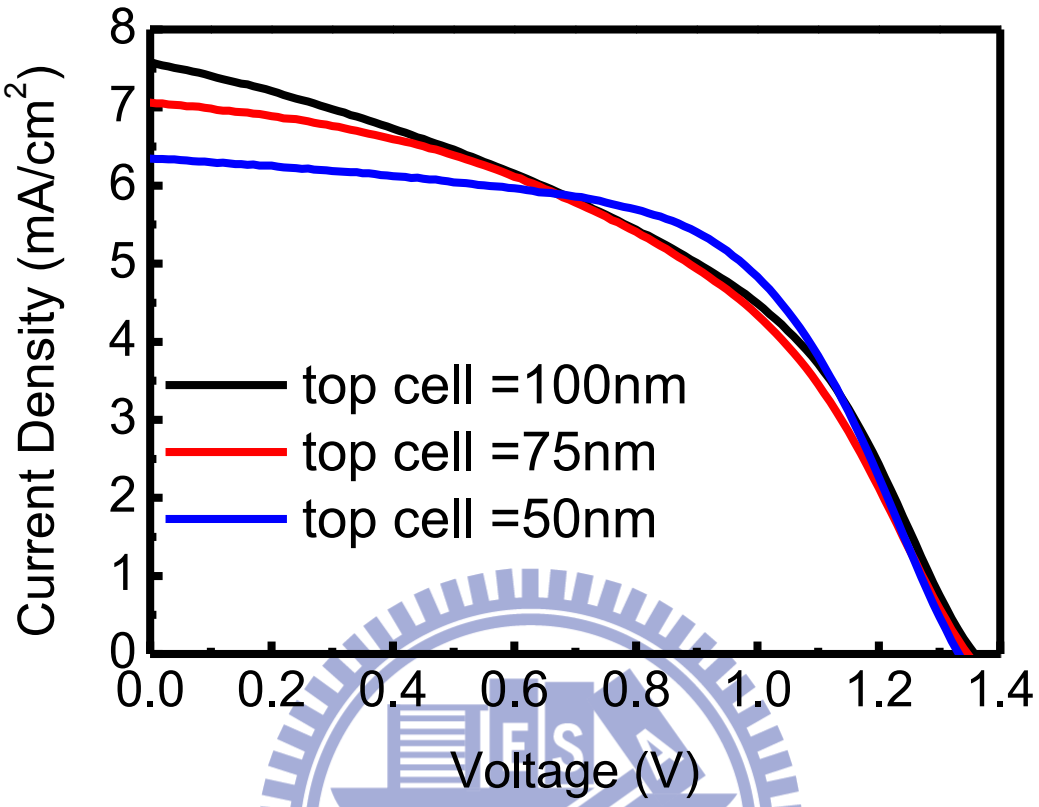

Figure 59 I-V Curve of a-Si/a-SiGe Tandem Solar Cell Varying i-layer Thickness on Top Cell

5.3.3 a-Si/a-Si/a-SiGe Triple Junction Solar Cell

The reason I fabricated a-Si/a-Si/a-SiGe triple junction solar cell was that I wanted to know if I used the same approach to combine three single junction into a triple junction solar cell, we would get the higher open circuit voltage. The following result was the only one triple junction I had ever tried. The structure is liked **Figure 60**. According to the experiment we have ever met, the doping concentration of n-layer should be lower which was about 1~1.5%. The result shows that the open circuit voltage is very high, which has achieved 2.07V and the FF has well performance. The only regret is that the short circuit current is too low to achieve high conversion efficiency. We could optimize the triple junction solar cell by fine tuning the i-layer and the pn layer of each junction.

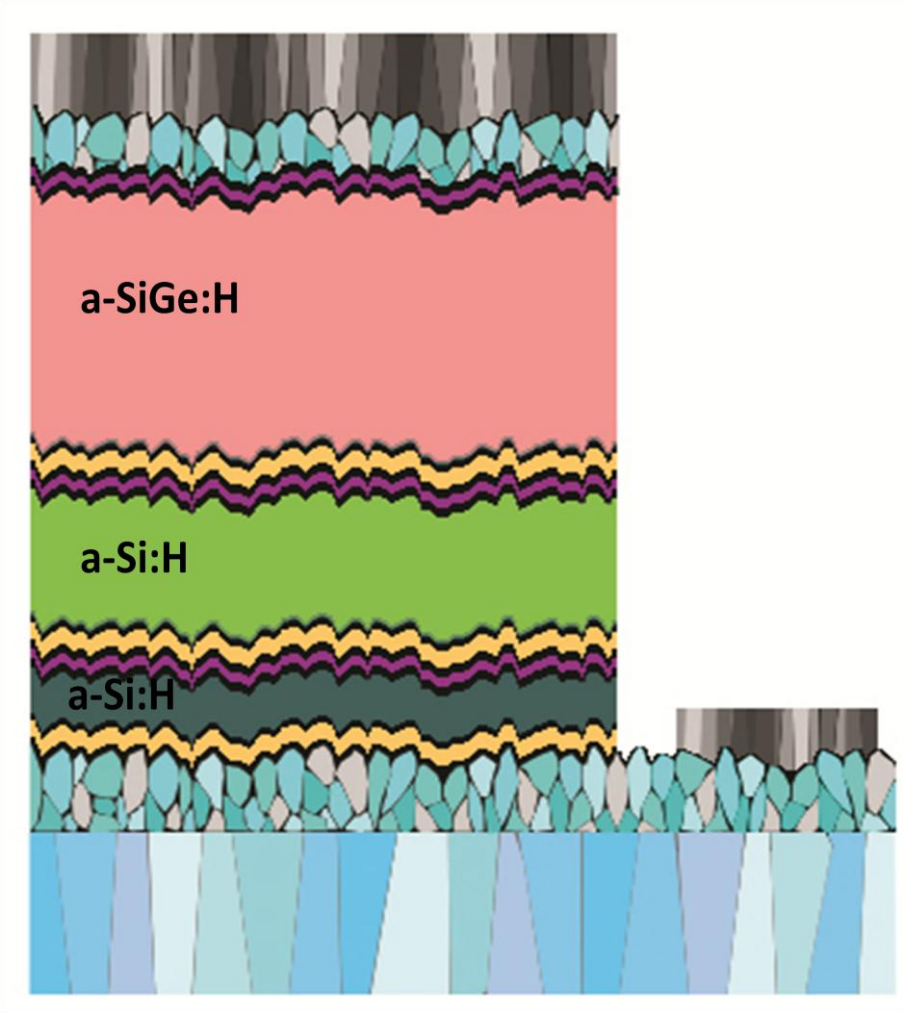

Figure 60 Structure of a-Si/a-Si/a-SiGe Triple Junction Solar Cell

SiH_4-GeH_4:H_2	i-layer Thickness	pressure	power	V_{oc}	J_{sc}	FF	η
sccm	nm	mtorr	40	(volt)	(mA/cm^2)	(%)	(%)
top cell	15:150	50	1.5	2.07	2.8	67.3	3.9
middle cell	15:150	75	1.5				
bottom cell	10-2:250	150	5				

Table 9 Result of a-Si/a-Si/a-SiGe Triple Junction Solar Cell

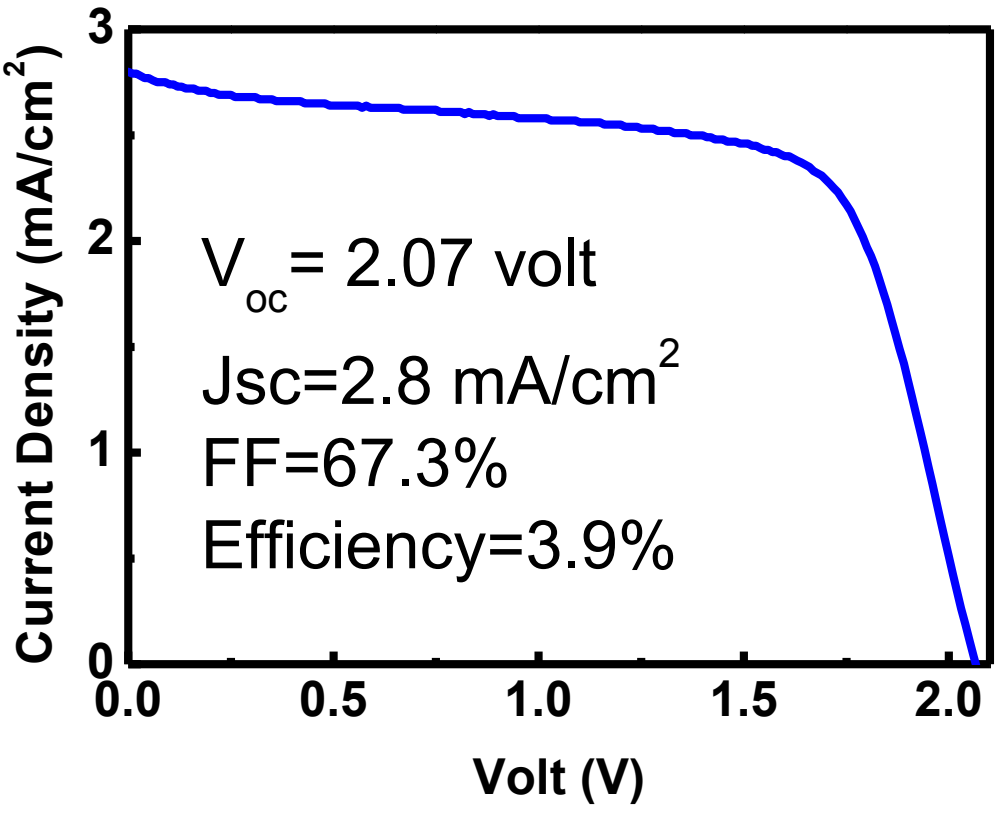

Figure 61 I-V Curve of a-Si/a-Si/a-SiGe Triple Junction Solar Cell

5.4 Conclusion and Future Work

We have fabricated silicon-based alloy thin film solar cell by using high density plasma method, including a-Si, a-SiC, a-SiGe, a-Si/a-SiGe, a-Si/a-Si, a-Si/a-Si/a-SiGe thin film solar cell. The conversion efficiency of each type of solar cell is as the following table.

Type of Solar Cell	a-Si single junction solar cell	a-SiC single junction solar cell	a-SiGe single junction solar cell
Conversion Efficiency	8.7%	7.98%	7.16%
Type of Solar Cell	a-Si/a-SiGe tandem solar cell	a-Si/a-Si tandem solar cell	a-Si/a-Si/a-SiGe triple junction solar cell
Conversion Efficiency	4.91%	6.53%	3.90%

Table 9 Conversion Efficiency of Each Type of Solar Cell

We have successfully developed the a-SiGe, tandem and triple junction solar cell with appropriate open circuit voltage. In the future, my research will focus on a-SiGe with high GeH_4/SiH_4+GeH_4 Ratio which could absorb more broadband in solar spectra and tunneling junction to reduce the recombination and upgrade short circuit performance.

Reference

[1] S. Sze and K. Ng, *Physics of semiconductor devices*: Wiley-Blackwell, 2007.

[2] C. Henry, "Limiting efficiencies of ideal single and multiple energy gap terrestrial solar cells," *Journal of applied physics,* vol. 51, p. 4494, 1980.

[3] J. Nelson, *The physics of solar cells*: World Scientific Pub Co Inc, 2003.

[4] A. R. Forouhi and I. Bloomer, "Optical dispersion relations for amorphous semiconductors and amorphous dielectrics," Physical Review B, vol. 34, p. 7018, 1986.

[5] J. Tauc, "Optical properties and electronic structure of amorphous Ge and Si," Materials Research Bulletin, vol. 3, pp. 37-46, 1968.

[6] N. No, "Fabrication and Characterization of Advanced Triple-junction Amorphous Silicon Based Solar Cells."

[7] T. Kamei and T. Wada, "Oxygen impurity doping into ultrapure hydrogenated microcrystalline Si films," Journal of applied physics, vol. 96, p. 2087, 2004.

[8] J. Woerdenweber, et al., "Influence of base pressure and atmospheric contaminants on a-Si: H solar cell properties," Journal of applied physics, vol. 104, p. 094507, 2008.

[9] T. Kilper, et al., "Oxygen and nitrogen impurities in microcrystalline silicon deposited under optimized conditions: Influence on material properties and solar cell performance," Journal of applied physics, vol. 105, p. 074509, 2009.